buildings

MDPI

Article

Size Effect of Slender and Thick Reinforced Concrete Members Without Transverse Reinforcement Failing in Shear: Parameter Analyses and Code Predictions

Gabriel Ferreira Girotto [1], Ana Laura Shiraga Araújo [1], Lisiane Pereira Prado [1], Eva Olivia Leontien Lantsoght [2,3,4], Eloi Figueiredo [5,6] and Alex Micael Dantas de Sousa [1,*]

1 School of Engineering, São Paulo State University (UNESP), Ilha Solteira 15385-007, SP, Brazil; g.girotto@unesp.br (G.F.G.); ana.shiraga@unesp.br (A.L.S.A.); lisiane.prado@unesp.br (L.P.P.)
2 Decanato de Investigación, Universidad San Francisco de Quito (USFQ), Quito 170901, Ecuador; elantsoght@usfq.edu.ec
3 Engineering Structures, Delft University of Technology (TU Delft), 2628 CD Delft, The Netherlands
4 Division of Structural Engineering, Luleå University of Technology, SE-971 87 Luleå, Sweden
5 Faculty of Engineering, Lusófona University, Campo Grande 376, 1749-024 Lisboa, Portugal; eloi.figueiredo@ulusofona.pt
6 CERIS, Instituto Superior Técnico, University of Lisboa, Av. Rovisco Pais 1, 1049-001 Lisboa, Portugal
* Correspondence: alex.dantas@unesp.br

Abstract

The shear strength of reinforced concrete members without transverse reinforcement remains a critical design issue, particularly for thick and slender structural members where pronounced size effects may significantly reduce the nominal shear strength. This study investigates the combined influence of member depth, concrete compressive strength, and longitudinal reinforcement ratio on the shear capacity of beams without stirrups through nonlinear finite element analyses (NLFEA). Beam depths ranging from 1000 mm to 4000 mm and concrete strengths between 30 MPa and 50 MPa were considered, together with variations in different longitudinal reinforcement ratios. The numerical results confirmed a clear deterministic size effect, with nominal shear stresses decreasing systematically as the effective depth increased, while the influence of compressive strength was found to be secondary. The depth-dependent response was successfully represented using Bažant's energetic Size Effect Law (SEL Type II), and the calibrated parameters provided an excellent fit to the numerical database. Furthermore, the numerical predictions of shear capacity were compared with major design provisions, including ACI 318 (2014 and 2019), Eurocode 2 (EN 1992-1-1:2005 and EN 1992-1-1:2023), and fib Model Code approaches with levels of approximation (LoA) 1 and 2. The results highlight that older formulations such as ACI 318-2014 and EN 1992-1-1:2005 tend to be unconservative for deep members, whereas EN 1992-1-1:2023 offers significantly improved agreement with reduced scatter. Among the evaluated expressions, *fib* Model Code LoA1 was the most conservative, while LoA2 provided the most accurate overall predictions. The findings emphasize the importance of incorporating size-effect considerations in modern shear design models, particularly for large reinforced concrete structures such as bridge decks, thick slabs, and dam walls.

Keywords: reinforced concrete; shear strength; finite element modeling; Concrete Damaged Plasticity; deep beams; design codes

Check for updates

Academic Editor: Vipul Patel

Received: 17 February 2026
Revised: 13 March 2026
Accepted: 18 March 2026
Published: 20 March 2026

 https://doi.org/10.3390/buildings16061234

1. Introduction

The shear strength of thick (greater than 1 m) reinforced concrete slabs or walls without transverse reinforcement is often a critical concern in the design of structural elements such as foundations for high-rise buildings [1], dam walls [2], or tunnel linings [3]. Additionally, thick reinforced concrete members without transverse reinforcement may be found in bridge deck slabs [4–6] and in nuclear facilities [7,8]. Among the main concerns when designing such structures for shear is that these are commonly designed in such a way that shear reinforcement shall be suppressed to avoid reinforcement congestion. Consequently, brittle failure modes may happen at ultimate limit states in shear [9–11].

Another cause for concern in thick members is the size effect in shear [12–14]. In practice, the size effect means that the nominal shear strength v decreases with increasing member thickness, a phenomenon which may be explained by an energetic size effect law (SEL Type II) proposed by Bažant [15–18] (Figure 1a—non-linear fracture mechanics). In practice, conducting experimental studies to better understand this phenomenon and improve the accuracy of analytical expressions provided by design codes is essential. However, testing full-scale structures faces significant challenges due to the weight, strength, and high cost involved in assembling such specimens [19–22]. For this reason, the problem is frequently investigated on slab strips (beam-shaped members), assuming that the member width does not significantly influence the shear capacity (Figure 1b).

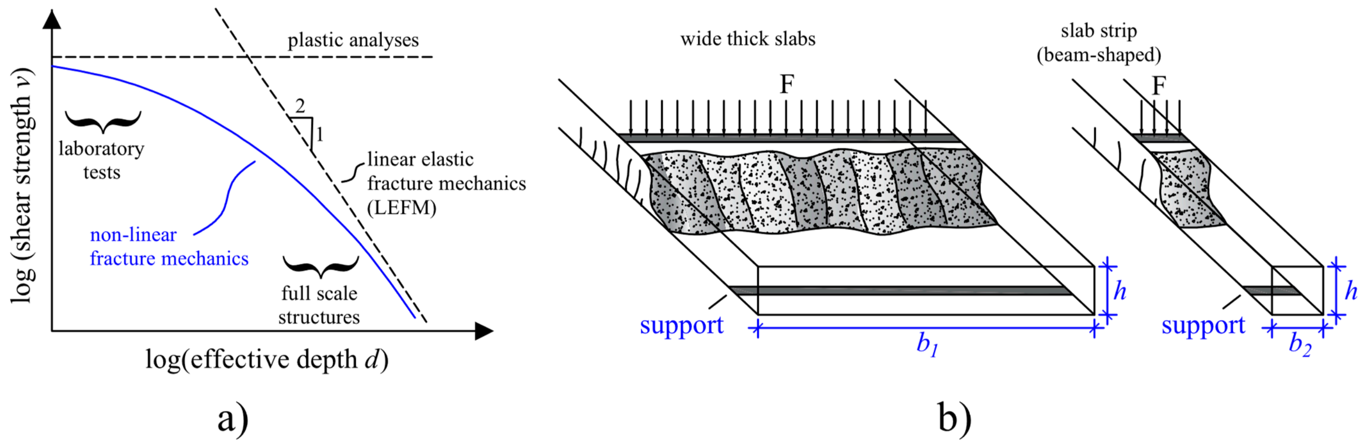

Figure 1. (**a**) Size effect in one-way shear (redrawn by the authors based on the concept of Bazant [15]); (**b**) transition from wide thick slabs to beam-shaped cross sections.

In the literature, it is noted that experiments addressing the shear capacity of beams with a significant depth (h > 1 m) often use short beams (a/d < 2, where a is the shear span defined as the distance between axes of load and support and d is the effective depth of the longitudinal reinforcement)[23,24], which are frequently evaluated using strut-and-tie models. In other words, the number of test results of slender beams failing in shear with a significant depth and a shear slenderness a/d > 2 is limited [21,25].

Another challenge in the size-effect investigation is the crowding of test results in databases associated with small-sized specimens, which may influence the weighting of size-effect correction factors in traditional comparisons of tested and predicted resistances using code expressions. In this context, for instance, Yu et al. [18] conducted a comprehensive comparison of the principal analytical models addressing the size effect on the shear strength of reinforced concrete beams, employing statistical filtering of experimental databases. In this way, it was possible to correct the bias related to the crowding of data on small-sized specimens from most databases published on this topic [13,25]. Nevertheless, it also highlighted that the existing data on slender beams with considerable depth were obtained under specific concrete strength and reinforcement ratios. Therefore, numerical methods could be employed to evaluate the impact of different parameters on the problem.

In the last decade, several design code provisions were updated regarding the shear capacity provisions with significant changes [26,27]. In practice, most of the international code provisions now include parameters related to the size effect. Nevertheless, in the calibration and validation of such codes, the accuracy of the expressions was always evaluated using databases with most beam depths lower than 1 m [28–31], in such a way that the size effect in shear was not a governing aspect. Therefore, further investigations should evaluate the accuracy level of code provisions for datasets of thick members.

In parallel with physics-based numerical simulations, recent studies have explored the use of machine learning and deep learning techniques to predict the structural behavior [32,33] and shear strength of reinforced concrete members [34–37]. Data-driven approaches have demonstrated promising results in capturing complex nonlinear relationships between geometric parameters, material properties, and structural responses, particularly when large experimental or numerical databases are available. Recent works have also applied deep learning frameworks to problems such as shear strength prediction, size-dependent behavior modeling, and automated identification of structural failure mechanisms (e.g., [33,34,38,39]). These approaches can improve predictive accuracy compared with traditional empirical formulations and may significantly reduce computational costs when used as surrogate models for complex numerical simulations. Nevertheless, the reliability of deep learning models strongly depends on the quality, representativeness, and physical consistency of the datasets used for training, which remain limited for large-scale reinforced concrete members failing in shear. In this context, high-fidelity nonlinear finite element analyses (NLFEA) can play a complementary role by generating physically consistent datasets that support the development and validation of data-driven models.

Thus, this study proposes (i) to investigate the accuracy level of a modelling strategy based on the Concrete Damaged Plasticity model (CDP) to represent the size effect in shear of reinforced concrete members without stirrups; and (ii) to evaluate the impact of recent design codes updating on the predictions of shear capacity of thick and slender reinforced concrete members without stirrups. To address this, a modeling strategy was first validated against shear failure tests from the literature with varying depths, from small to large beams. After, parametric analyses were performed varying the beam height, concrete compressive strength and longitudinal reinforcement ratio of the beams. At the end, the measured shear capacity on the numerical models was compared to that predicted by different design codes. Additionally, the numerical results were evaluated in light of the Bazant size-effect law to identify the impact of the evaluated parameters (material properties and reinforcement ratio) on shear size effect.

Unlike previous publications in this field, which proposed simulating concrete behavior with total strain crack models (DIANA) [40,41], fracture-plastic constitutive model (ATENA), microplane constitutive model [17,42], user material models (UMATS) [43], this paper investigates the accuracy of using the Concrete Damaged Plasticity (CDP) model available in ABAQUS to describe the concrete nonlinear behavior. Therefore, this paper may provide an important framework for modelling full-scale structures subjected to significant size effects in shear using the CDP model.

2. Test Results for Validation of the Modeling Strategy

In this study, different test results from the literature were used to validate the proposed modelling approach [3,21,22]. These tests included different load types (using 1 or 2 concentrated loads—Figure 2), shear slenderness *a/d* around 3, which means that these members can be classified as slender members in shear, and no arching action influenced the shear failure [13].

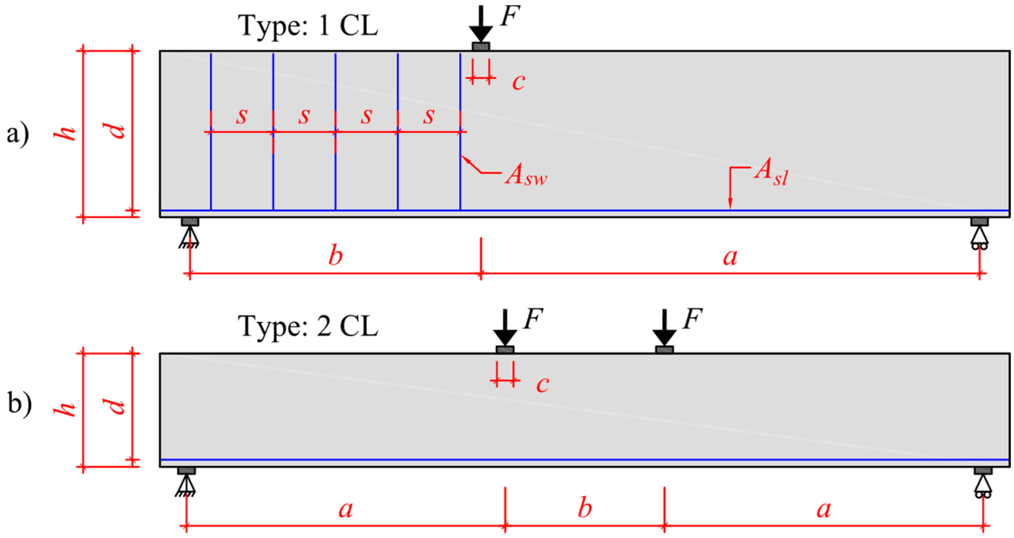

Figure 2. Geometry of the test specimens used for validation: (**a**) Type 1 CL configuration; (**b**) Type 2 CL configuration.

Table 1 presents the main geometric information from 6 tests used to validate the modelling approach. The tests were performed by Collins et al. [3], Syroka et al. [21] and Zhai and Moehle [22] and include beams with heights ranging from 200 mm to 4000 mm. Consequently, the selected tests enabled us to assess whether the proposed numerical model could simulate the size effect in one-way shear.

Table 1. Geometry of test results for validation of the modelling approach.

Size	Author	Load Type	Test	h (mm)	b_w (mm)	l_{span} (mm)	a (mm)	b (mm)	c (mm)	d (mm)
Large	Collins et al. [3]	1 CL	PLS4000	4000	250	19,000	12,000	7000	400	3840
Large	Zhai and Moehle [22]	1 CL	UCB 1	3550	254	21,300	10,650	10,650	305	3291
Small	Collins et al. [3]	1 CL	PLS300	300	250	1650	825	825	38	264
Small	Syroka-Korol et al. [21]	2 CL	SL20	200	220	1200	480	240	60	160
Small	Syroka-Korol et al. [21]	2 CL	SL40	400	220	2700	1080	540	120	360
Small	Syroka-Korol et al. [21]	2 CL	SL80	800	220	5625	2250	1120	120	750

In turn, Table 2 details the longitudinal reinforcement in the tests. At this point, it shall be noted that the longitudinal reinforcement ratio in the tests varied from 0.46% to 0.90%, which represents a most representative range of flexural reinforcement for most thick slabs without transverse reinforcement in practice, mainly for bridges [44]. In addition, Table 2 also describes the transverse reinforcement ratio applied in the tests on which one of the beam sides was shear reinforced to promote the shear failure at the opposite side.

It should be noted that the experimental validation performed in this study relies on a limited number of tests, which represents a common constraint in research involving large-scale reinforced concrete members subjected to shear-dominated failure [3,21,22]. Therefore, the proposed modelling strategy was validated only for beams of normal-strength concrete with thicknesses ranging from 300 mm to 4000 mm and shear slenderness $a/d \geq 3$.

Table 2. Reinforcement information and material properties.

Author	Test	A_{sl} (mm^2)	ρ_l (%)	f_y (MPa)	A_{sw} (mm^2)	s	ρ_w (%)	f_{yw} (Mpa)	f_{cm} (MPa)	d_{ag} (mm)
[3]	PLS4000	6362	0.66%	573	3.14	150	0.084%	522	40	14
[22]	UCB 1	3855	0.46%	820	1.91	89	0.085%	420	32	19
[3]	PLS300	301	0.65%	458	-	-			44.8	14
[21]	SL20	314	0.89%	500	-	-		-	35	16
[21]	SL40	716	0.90%	500	-	-		-	35	16
[21]	SL80	1492	0.90%	500	-	-		-	35	16

Notes: [3] = Collins et al. (2015); [22] = Moehle and Zhai; [21] = Syroka-Korol et al. (2014).

3. Proposed Modelling Approach

3.1. General Description

In this study, two-dimensional numerical models were developed in ABAQUS/Standard to simulate shear failure. The finite element analyses were conducted on a workstation equipped with an Intel Core i9-14900K CPU (24 cores, 32 threads) and 32 GB RAM. The average computational time for each numerical model was approximately 30 min.

In the numerical models, the simplification of representing only the resulting longitudinal reinforcement position, rather than modeling all reinforcement layers, was adopted. Figure 3 illustrates the geometric configuration and reinforcement layout of the test PLS4000 from Collins et al. [3].

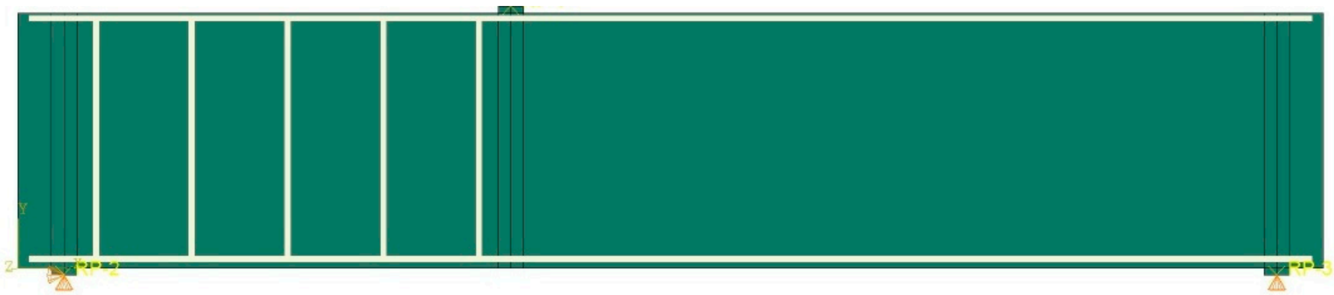

Figure 3. Overview of the numerical model.

3.2. Mesh

For the concrete parts and steel plates, S4 finite elements were used, which are quadrilateral shell elements with four nodes each, with six degrees of freedom (three translational and three rotational). These elements allow linear approximations of the displacement and rotational fields at the nodes. For the reinforcement bars, T2D2 elements were adopted, which are two-dimensional truss elements with two end nodes and linear interpolation of nodal displacements.

The size of the finite elements varied according to the beam height. In this study, this size was chosen to ensure at least 20 elements along the beam height, such as performed by Luo et al. [42] in a beam 400 mm height. Therefore, the finite element size varied from 200 mm in test PLS4000 to 10 mm in the test SL20. In practice, this variable finite element size allows for reaching almost the same density of finite element despite of the beam size. Figure 4 shows the finite element mesh discretization used in the numerical model corresponding to the test PLS4000 from Collins et al. [3].

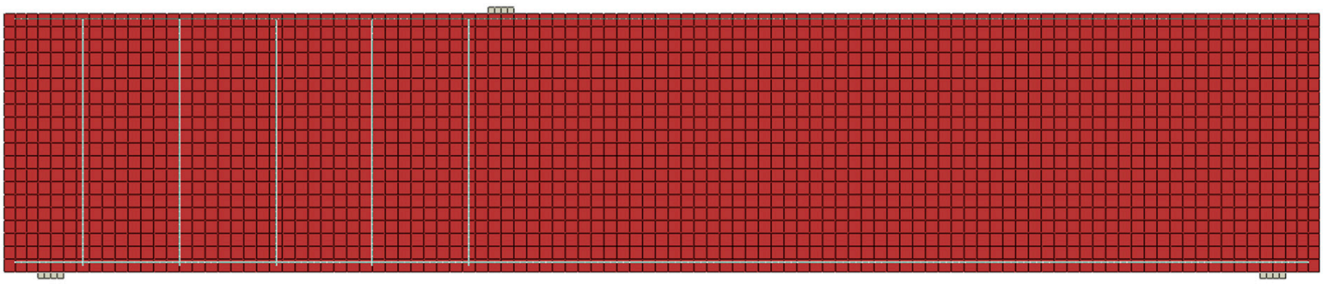

Figure 4. Mesh discretization.

3.3. Interactions

A perfect bond between the reinforcement and the concrete was assumed in the numerical simulations, as no anchorage failure was observed in the tests. This property was implemented using the embedded constraint tool available in ABAQUS.

For the interface between the steel plates and the concrete beam, a tangential behavior was defined using a penalty formulation (with a friction coefficient of 0.5), and a normal behavior was defined as rigid (hard contact), allowing separation between the two surfaces to prevent tensile stress at the supports.

In both the loading and support plates, rigid-body interactions were defined between each plate and a master node at its center (here referred to as reference points, or RPs—Figure 5). These interactions enabled the assignment of boundary conditions to the plate reference points, facilitating the application of constraints and providing a more accurate representation of the pinned connections at these locations.

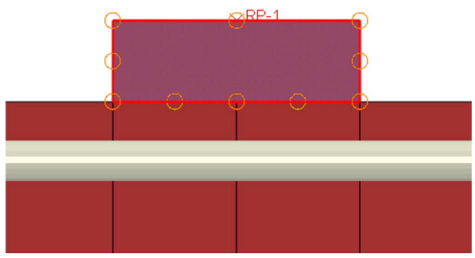

Figure 5. Selected parts in the definition of the rigid body interaction between the loading plate and the reference point RP-1.

3.4. Boundary Conditions

Vertical and horizontal displacements were restrained at the left support, while only vertical displacements were restrained at the right support (Figure 6). Rotations at the supports were left unrestrained to allow for pinned connection behavior. A prescribed vertical displacement of 25 mm was applied at the center of the loading plate to simulate a displacement-controlled loading. This approach enabled assessment of the beam's load-carrying capacity (maximum force) and post-peak behavior.

(**a**) (**b**)

Figure 6. Boundary conditions applied at the supports: (**a**) left and (**b**) right of the numerical models.

3.5. Steps of the Loading

Unlike other numerical studies on shear and punching [45–47], the consideration of self-weight in this type of problem is fundamental, as the portion of the load generated by self-weight in the model is significant. For this reason, all simulations were carried out in two stages (STEPS) to better represent the experimental tests. In the first stage, only the self-weight was applied to the beams; in the second stage, a concentrated load was applied through a prescribed displacement at the center of the loading plate. This procedure was necessary because, at the onset of the concentrated load application, the self-weight component should already be acting at its full value (as observed in the tests). If both loadings (self-weight and concentrated load) were applied in a single stage, the model could fail at a load level at which the full self-weight had not yet acted. The self-weight was accounted for in the numerical simulations by including the gravitational acceleration g and assuming a reinforced concrete density of 2500 kg/m^3.

3.6. Solution Procedure

The nonlinear analyses were performed using the implicit solver available in ABAQUS/Standard, adopting a Static, General step under quasi-static conditions. Automatic time incrementation was enabled to ensure numerical robustness during the simulation of nonlinear material behavior. The maximum increment size was limited to 1.0×10^{-4}, while the minimum allowable increment size was set to 1.0×10^{-15}, allowing the solver to adequately capture stiffness degradation and potential convergence difficulties associated with cracking and softening phenomena.

A direct equation solver was employed, with unsymmetric matrix storage selected. The nonlinear equilibrium equations were solved using the Full Newton–Raphson method, ensuring consistent updating of the tangent stiffness matrix at each iteration. The maximum number of iterations allowed before reforming the kernel matrix was set to eight, following the default ABAQUS configuration.

Severe discontinuity iterations were handled by propagating information from the previous step, as defined by the ABAQUS default settings. Loads were applied using a linearly ramped amplitude over the step, avoiding instantaneous load application and improving convergence in the presence of nonlinearities. Linear extrapolation of the solution state from the previous increment was adopted at the start of each increment to enhance convergence efficiency.

3.7. Material Properties

Concrete was represented using the Concrete Damaged Plasticity (CDP) model available in ABAQUS, which is grounded on three fundamental components [48]: (i) the description of uniaxial stress–strain behavior, (ii) the definition of the yield surface, and (iii) the specification of the plastic flow rule. The damage formulation governs the progressive reduction in the initial elastic stiffness E_0 as strains increase. The yield surface follows the formulation originally proposed by Lubliner [49], later enhanced by Lee and Fenves [50]. Plastic flow within the CDP framework is described using a non-associated flow rule, in which the plastic potential function G is defined by a hyperbolic Drucker–Prager-type expression [51]. A comprehensive description of the mathematical formulation of the CDP model can be found in the literature [52].

In the CDP model, the shear response is not defined through an independent constitutive law. Instead, shear behavior emerges from the multiaxial plasticity formulation governing the concrete yield surface [53]. The model adopts a Drucker–Prager type yield function combined with isotropic damage variables that describe stiffness degradation under tensile and compressive loading. Consequently, the shear strength of the material is governed by the stress state and by parameters controlling the shape of the yield surface, such as the dilation angle, the ratio between biaxial and uniaxial compressive strength, and the eccentricity parameter. Degradation of the shear stiffness occurs indirectly through the evolution of tensile and compressive damage variables. Detailed descriptions of the formulation and its implications for shear-dominated problems can be found in Lubliner et al. [49], Lee and Fenves [50], and the ABAQUS documentation [48].

The elastic modulus of concrete was estimated according to the equations provided by the fib Model Code 2010 [54]:

$$E_c = \alpha_i \cdot E_{ci} \tag{1}$$

$$E_{ci} = \alpha_E \cdot 21500 \cdot \left(\frac{f_{cm}}{10}\right)^{1/3} \tag{2}$$

$$\alpha_i = 0.8 + 0.2 \cdot \frac{f_{cm}}{88} \tag{3}$$

where E_c is the reduced elastic modulus of concrete at a stress level of approximately 40% of f_{cm}, E_{ci} is the initial or tangent modulus at the origin of the stress–strain curve, and α_E is a coefficient accounting for the type of coarse aggregate used in the concrete (taken as 1 for granite aggregates).

The compressive stress–strain response of concrete was defined in accordance with the formulations recommended by the fib Model Code 2010 [54]:

$$\sigma_c(\varepsilon_c) = f_{cm} \cdot \frac{k \cdot \eta - \eta^2}{1 + (k-2) \cdot \eta} \tag{4}$$

$$k = 1.05 \cdot E_c \cdot \frac{\varepsilon_{c1}}{f_{cm}} \tag{5}$$

$$\eta = \frac{\varepsilon_c}{\varepsilon_{c1}} \tag{6}$$

where

$$\varepsilon_{c1} = 0.7 \cdot \frac{f_{cm}{}^{0.31}}{1000} \tag{7}$$

In tension, the concrete uniaxial behavior was modeled using stress–crack-opening ($\sigma_t \times w$) relationships to reduce mesh sensitivity in the results. In this study, the $\sigma_t \times w$ relationship was modeled according to the model proposed by Hordijk [55]:

$$\sigma_t(w) = f_{ct} \cdot \left\{ \left[1 + \left(c_1 \cdot \frac{w}{w_c}\right)^3\right] \cdot e^{-c_2 \cdot \frac{w}{w_c}} - \frac{w}{w_c} \cdot \left(1 + c_1^3\right) \right\} \tag{8}$$

$$w_c = 5.14 \cdot \frac{G_f}{f_{ct}} \tag{9}$$

With c_1 = 3 and c_2 = 6.93.

The fracture energy G_f and concrete tensile strength f_{ct} were calculated, in the absence of experimental data, according to the fib Model Code 2010 as:

$$f_{ct} = 0.3 \cdot (f_{cm} - 8)^{2/3} \tag{10}$$

$$G_f = 73 \cdot f_{cm}{}^{0.18} \tag{11}$$

In this case, the stress–crack opening curves were converted into stress–inelastic strain curves by dividing the crack opening values w by the characteristic finite element length l_{eq}

(i.e., the representative average size of the finite elements), as proposed by Genikomsou and Polak [52]:

$$\varepsilon_t = \frac{f_{ct}}{E_c} + \frac{w}{l_{eq}} \tag{12}$$

In the CDP, the following plasticity parameters were imputed: dilation angle $\psi = 40°$ (based on a calibration study grounded on the comparison between tested and predicted resistances, as in other publications [45,46,56]); shape factor $K_c = 0.66$ based on Wiliam & Warnke [57]; eccentricity $e = 0.1$ (default ABAQUS value [48]); biaxial-to-uniaxial compressive strength ratio $\sigma_{b0}/\sigma_{c0} = 1.16$ based on Kupfer [58,59]; and the viscosity parameter $\mu = 10^{-5}$ was used after sensibility study (also in line with other references to avoid numerical convergence issues without influencing the structural behavior [45]).

A sensibility study indicated that tensile fracture energy and dilation angle have the greatest influence on predicted shear resistance, whereas variations in the plasticity parameters (shape factor, eccentricity, and biaxial-strength ratio) have a comparatively smaller effect on the overall response, in line with previous investigations in this field [52,60].

The steel, in turn, was modeled using the Von Mises constitutive model, assuming a perfectly elastic-plastic behavior (bilinear stress–strain curve without hardening). Thus, the steel behavior was defined by specifying only the elastic modulus (E_s = 210,000 MPa) and Poisson's ratio (0.3), and by assigning the yield strength (f_y) based on the bar diameter.

Importantly, the calibration of the Concrete Damaged Plasticity (CDP) parameters was not performed specifically to fit the selected validation tests, but was based on values commonly adopted in the literature [45,46,56,61,62] and on previously validated constitutive relationships for concrete in tension and compression [45,46]. This approach was adopted to reduce potential circularity between calibration and validation. Nevertheless, numerical modelling of shear-dominated behavior inherently involves uncertainties related to parameters such as fracture energy and dilation angle [45,46,56]. Therefore, these modelling uncertainties may influence the absolute values predicted by NLFEA. Nonetheless, while the quantitative values should be interpreted with caution, the observed trends are considered robust within the modelling framework adopted.

4. Validation of the Numerical Modeling Strategy

4.1. Ultimate Capacity

Figure 7 compares the experimental result with the numerical model prediction for the force-displacement curve. In general, the numerical model adequately represented the experimental beam's stiffness, maximum force, and the abrupt force drop at the moment of failure, which characterizes brittle shear failure mechanisms. This correspondence highlights the numerical model's accuracy in capturing the beam's response phases under loading.

Table 3 compares the experimentally measured ultimate loads with those predicted by the finite element model (FEM) for reinforced concrete members covering a wide range of depths, from 200 mm to 4000 mm, and longitudinal reinforcement ratios between 0.46% and 0.90%. Overall, the FEM predictions show very good agreement with the experimental results, with an average ratio F_{EXP}/F_{FEM} equal to 0.99 and a coefficient of variation of 6.07%, indicating both accuracy and low scatter.

Table 3. Comparison between experimental and predicted ultimate loads with the FEM.

Author	Test	h (mm)	ρ_l (%)	F_{EXP}/F_{FEM}
Collins et al. [3]	PLS4000	4000	0.66%	1.01
Zhai and Moehle [22]	UCB 1	3550	0.46%	0.93

Table 3. *Cont.*

Author	Test	h (mm)	ρ_l (%)	F_{EXP}/F_{FEM}
Collins et al. [3]	PLS300	300	0.65%	1.01
Syroka-Korol et al. [21]	SL20	200	0.89%	1.09
Syroka-Korol et al. [21]	SL40	400	0.90%	0.96
Syroka-Korol et al. [21]	SL80	800	0.90%	0.94
			AVG	0.99
			COV (%)	6.07%

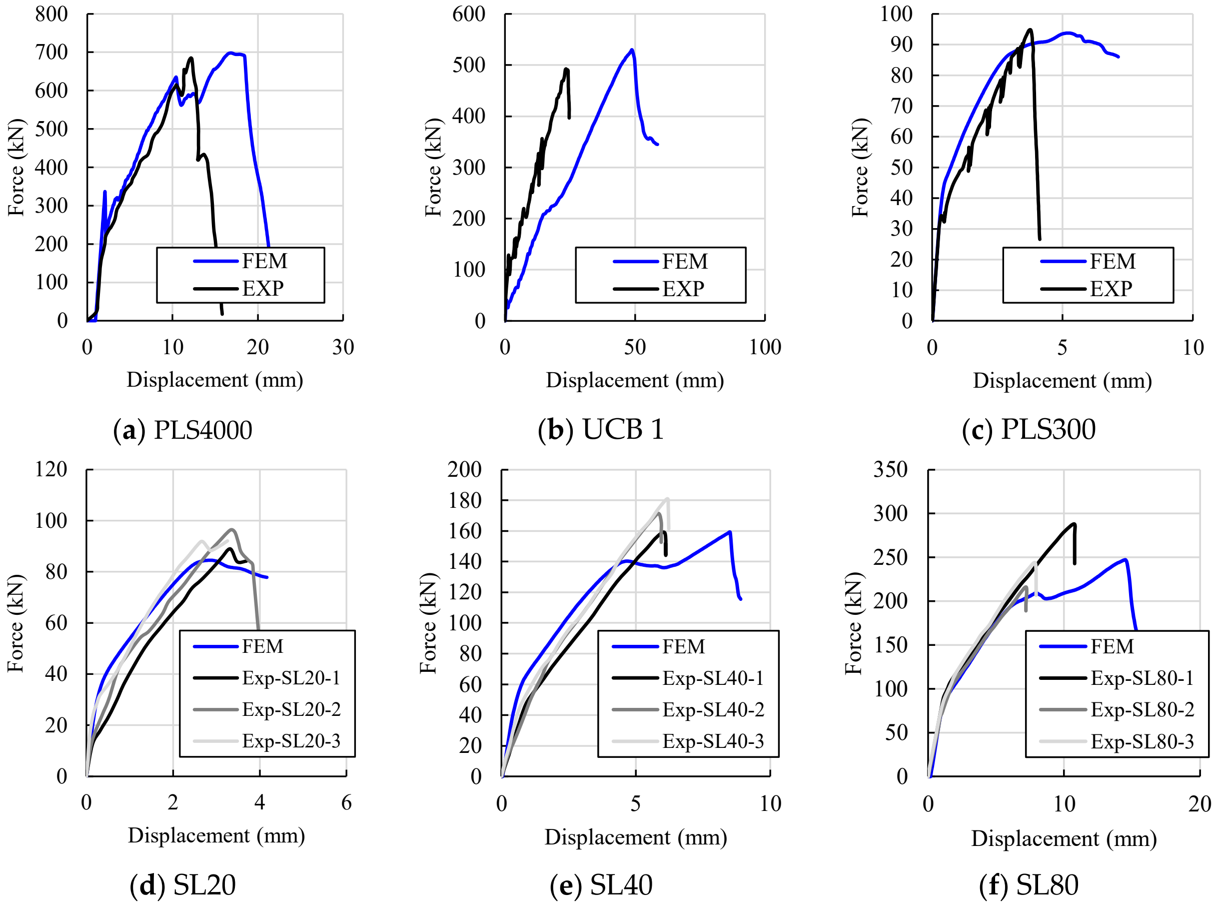

Figure 7. Comparison between experimental and numerical force–displacement graphs obtained from the FEM.

For the largest-scale specimen (PLS4000, $h = 4000$ mm), the FEM slightly underestimated the experimental ultimate load, yielding a ratio close to unity (1.01). This result demonstrates the capability of the numerical model to capture size-dependent mechanisms governing shear resistance in very thick members, where pronounced cracking, stress redistribution, and softening effects are expected to dominate the structural response. Similarly, the smaller PLS300 specimen ($h = 300$ mm) also exhibited excellent agreement, suggesting that the adopted modeling strategy remains consistent across markedly different structural scales. The tests reported by Zhai and Moehle (UCB 1) show a slightly more non-conservative FEM prediction ($F_{EXP}/F_{FEM} = 0.93$), which may be attributed to uncertainties related to the predicted concrete tensile strength and fracture energy [63]. In contrast, the specimens from Syroka-Korol et al. [21] display ratios ranging from 0.94 to 1.09, with no systematic trend with increasing depth. This absence of bias suggests that the

FEM does not introduce a depth-dependent overestimation or underestimation of strength within the investigated range.

Overall, the relatively narrow dispersion of results and the absence of clear systematic trends indicate that the proposed FEM framework is robust and consistently reproduces the ultimate load capacity of shear-critical reinforced concrete members. The close agreement between numerical and experimental results supports the suitability of the adopted constitutive models, solution strategy, and boundary condition definitions for simulating shear-dominated failure mechanisms in reinforced concrete elements.

4.2. Cracking Pattern

Figure 8 compares experimentally observed and numerically predicted cracking patterns for specimens with different depths and test configurations. Despite the significant variation in size and boundary conditions (1 and 2 concentrated loads), the numerical model consistently reproduces the key characteristics of the experimentally observed cracking behavior: (i) the numerical simulations capture the formation of inclined shear cracks extending from flexural cracks towards the load application region, which is also consistent with the Critical Shear Crack Theory (CSCT—[64]); (ii) the orientation and location of the critical shear cracks show good agreement with the experimental observations, indicating that the adopted constitutive formulation is capable of representing the stress redistribution and strain localization associated with shear-dominated responses.

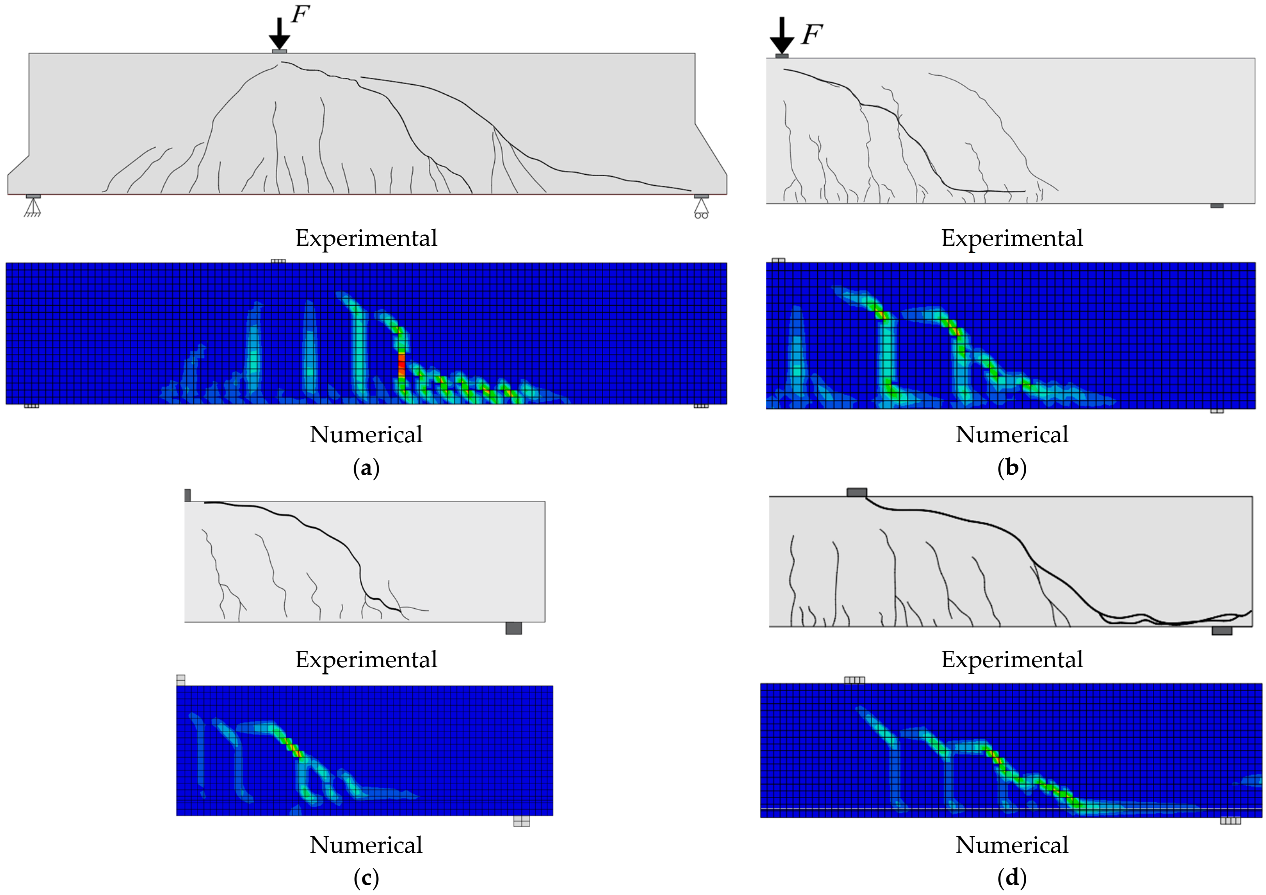

Figure 8. Comparison of experimental and numerically predicted cracking patterns for different specimens: (**a**) Collins et al. [3] (4 m test), (**b**) Zhai and Moehle [22], (**c**) Collins et al. [3] (0.30 m test), and (**d**) Sýkora et al. [21].

A clear size-dependent trend is also observed when comparing large and small-scale specimens. In the larger members, cracking tends to localize into a dominant inclined crack, whereas smaller specimens exhibit a more distributed cracking pattern prior to failure. This transition is well reproduced by the numerical model, demonstrating its ability to capture the influence of member depth on cracking localization and failure mode, a key aspect of shear behavior in reinforced concrete structures.

Nevertheless, some differences between experimental and numerical cracking patterns are also observed. For instance, the numerical cracks appear smoother and less discrete than those observed experimentally, particularly in terms of fine crack branching and local crack irregularities. These discrepancies are inherent to the smeared-crack approach adopted in continuum damage models such as CDP and are influenced by mesh resolution [49,65]. Because the concrete damage plasticity model employs a smeared crack formulation, cracking is represented through strain localization within the finite elements. Therefore, the predicted crack patterns provide qualitative insight into damage distribution but should not be interpreted as exact discrete crack trajectories. However, such limitations do not compromise the accurate prediction of crack orientation, localization, or global failure mode [66].

Regarding the influence of the cracking pattern on the shear transfer behavior, Cavagnis et al. [67,68] demonstrated that changing the shape of the critical shear crack changes the relative contribution of each shear transfer mechanism in the section (compression chord capacity, aggregate interlock, dowel action, residual tensile strength) on the shear capacity. Nevertheless, these authors also observed that tests with similar shear slenderness and material properties will reach similar levels of shear capacity, even when the shape of the critical shear crack varies in these tests. Therefore, minor differences between the predicted by the numerical model and observed cracking patterns in the tests (common on smeared-crack numerical models) can be considered secondary, as they will not influence the ultimate capacity significantly.

4.3. Sensibility Study

Figure 9 presents the sensitivity analysis performed to evaluate the influence of key numerical parameters on the predicted load–displacement response. In Figure 9a, the effect of the characteristic finite element length l_{eq} is investigated using element sizes of 100, 200, and 400 mm. Figure 9b shows the influence of the dilation angle of the Concrete Damaged Plasticity (CDP) model, considering values of 35°, 40°, and 45°. Finally, Figure 9c illustrates the effect of the viscosity parameter adopted for numerical regularization. The horizontal red line represents the experimental peak load F_{exp}, allowing a direct comparison between the numerical predictions and the experimental reference.

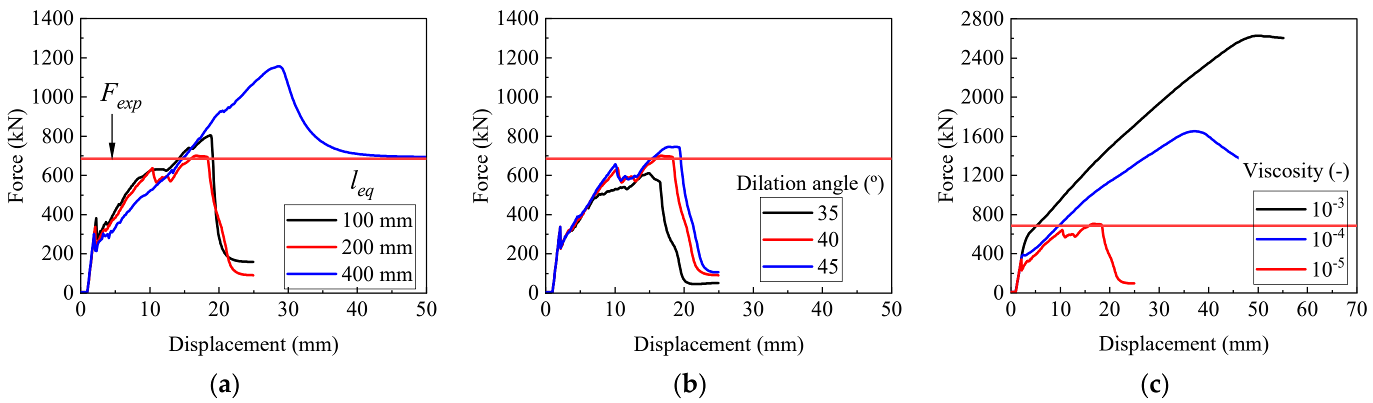

Figure 9. Sensitivity analysis of the numerical model showing the influence of (**a**) finite element size l_{eq}, (**b**) dilation angle, and (**c**) viscosity parameter of the Concrete Damaged Plasticity (CDP) model on the load–displacement response. The horizontal red line indicates the experimental peak load F_{exp}.

The results indicate that the numerical predictions are sensitive to the investigated modeling parameters. The characteristic element length, l_{eq}, significantly affects the post-peak response and peak load, with larger elements leading to higher peak forces and a smoother softening behavior (Figure 9a). In practice, this occurs because it is necessary to have a good number of finite elements distributed along the member height and, mainly, along the compression chord, to simulate the stress state in the fracture process zone that triggers the size effect. In this study, we observed that 20 elements distributed along the beam height would be sufficient to simulate the size effect behavior.

The dilation angle also influences the predicted strength, with higher values resulting in increased shear capacity, reflecting the enhanced shear transfer associated with volumetric expansion constrained in the struts (Figure 9b). In turn, although viscosity is a numerical parameter that facilitates solution convergence, it may have an undesirable influence on structural behavior when higher values are used, even blocking the size effect. As observed in previous investigations, a value of 10^{-5} seems sufficiently low to avoid any undesirable influence on material behavior [45,46].

4.4. Limitations of the Numerical Modelling Approach

Although the numerical models were validated against available experimental results, some modelling assumptions should be acknowledged. First, the simulations were performed using a two-dimensional representation of the structural members, thereby neglecting possible three-dimensional stress redistribution. Second, a perfect bond between reinforcement and concrete was assumed through the embedded reinforcement approach, thereby neglecting potential slip effects that may influence crack spacing and load transfer mechanisms.

In addition, the adopted continuum approach does not explicitly model aggregate interlock at the meso-scale, since concrete is represented as a homogeneous material using the concrete damage plasticity (CDP) model. Consequently, shear-transfer mechanisms are implicitly captured in the constitutive formulation rather than explicitly through aggregate interaction. Finally, the results are influenced by the fracture-energy parameters used to describe tensile softening, which controls crack localization and energy dissipation within the smeared-crack framework.

5. Parameter Analysis

5.1. Overview

In the present study, a comprehensive parametric analysis was carried out to investigate the influence of member depth, concrete compressive strength and longitudinal reinforcement ratio on the structural behavior of the beams (Figure 10). In this context, the geometry of the test PLS4000 from Collins et al. [3] was used as a reference. For the parametric analyses, three member heights were tested (h = 4 m, 2 m, and 1 m). In this member-depth variation, all geometry parameters were varied to keep the shear slenderness *a/d* constant (i.e., the test scale varied with the beam height). In addition, three concrete strength classes were considered: 30 MPa, 40 MPa, and 50 MPa. The corresponding concrete tensile strength f_{ct} and fracture energy G_f were calculated according to expressions (10) and (11), respectively (Section 3.7). In parallel, four different longitudinal reinforcement ratios were adopted, corresponding to 0.66%, 0.99%, 1.33%, and 1.66%. The combination of these parameters yielded 36 numerical models.

In this study, the values used in the parametric analyses were selected to span the range of member thicknesses, concrete classes, and reinforcement ratios properly in the validation dataset (Tables 1 and 2). In other words, for instance, the study did not extend to high-strength concrete because the proposed modelling strategy was validated only for normal-strength concrete beams.

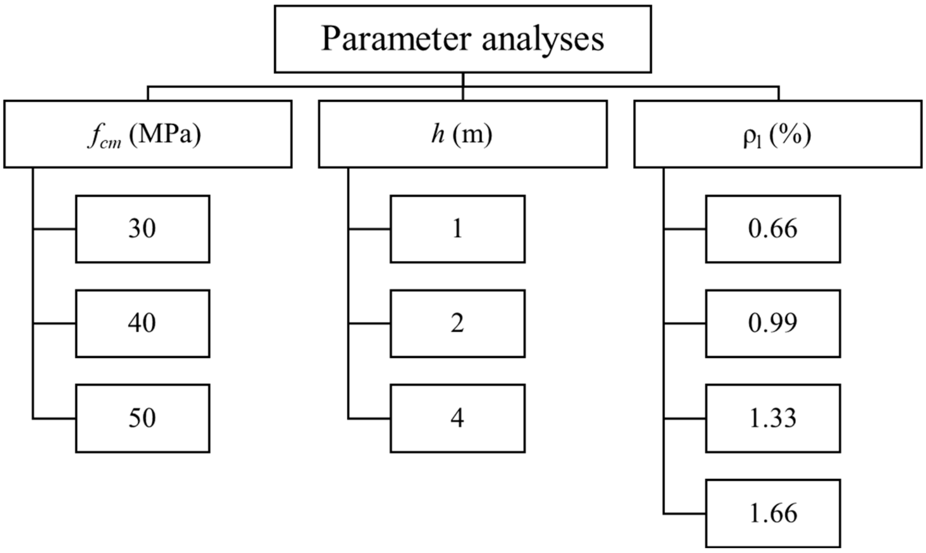

Figure 10. Overview of the parameter analyses.

5.2. Load-Deflection Response

Figure 11 presents the numerical force–displacement responses for members with different depths, concrete compressive strengths, and longitudinal reinforcement ratios λ. The observed trends are consistent with the fundamental assumptions of established shear theories, particularly the Critical Shear Crack Theory (CSCT) [69] and the Modified Compression Field Theory (MCFT) [70,71].

According to the CSCT, the shear resistance of reinforced concrete members without transverse reinforcement is governed by the development and progressive opening of a critical shear crack, whose width increases with structural deformation and member depth [69,72]. As a result, larger members are expected to exhibit reduced stiffness, lower nominal shear strength, and a more pronounced post-peak softening response. This behavior is clearly reflected in numerical results: increasing the depth from 1 m to 4 m leads to flatter ascending branches and extended post-peak softening, indicating a failure process controlled by crack opening rather than by reaching a fixed material strength.

The influence of concrete compressive strength f_{cm} observed in the numerical simulations is also consistent with CSCT predictions. While higher values of f_{cm} systematically increase the peak load for all member depths, they do not eliminate the size-dependent reduction in stiffness and strength. This agrees with CSCT formulations, in which concrete strength contributes to shear resistance but cannot compensate for the increase in critical crack width associated with larger structural dimensions [69].

From the perspective of the MCFT, shear resistance is governed by strain-dependent mechanisms involving cracked concrete in compression, aggregate interlock, and the tensile response of the longitudinal reinforcement [71]. The numerical force–displacement curves show that larger members reach peak load at higher deformation levels and exhibit more gradual stiffness degradation, which is consistent with MCFT predictions of reduced shear capacity under increasing strain demand. The extended softening branches observed for larger depths reflect the progressive degradation of aggregate interlock and compression softening effects explicitly accounted for in the MCFT framework [70].

The role of the longitudinal reinforcement ratio is particularly evident in the numerical results. Increasing ρ_l leads to higher stiffness and increased peak load across all depths, with the effect becoming more pronounced for larger members. Within the CSCT framework, this behavior can be attributed to the ability of higher longitudinal reinforcement ratios to restrain crack opening, thereby delaying the attainment of a critical crack width [69]. Similarly, within the MCFT, higher ρ values reduce longitudinal strain levels, which enhances aggregate interlock and the capacity of the compression field, resulting in increased shear resistance [71].

However, the numerical results also indicate that higher values of ρ are associated with a steeper post-peak response, particularly for the largest members. This trend suggests a more brittle failure process once the critical crack becomes unstable, which is consistent with CSCT expectations that stronger crack-bridging mechanisms may increase peak resistance but lead to a sharper strength drop after peak load.

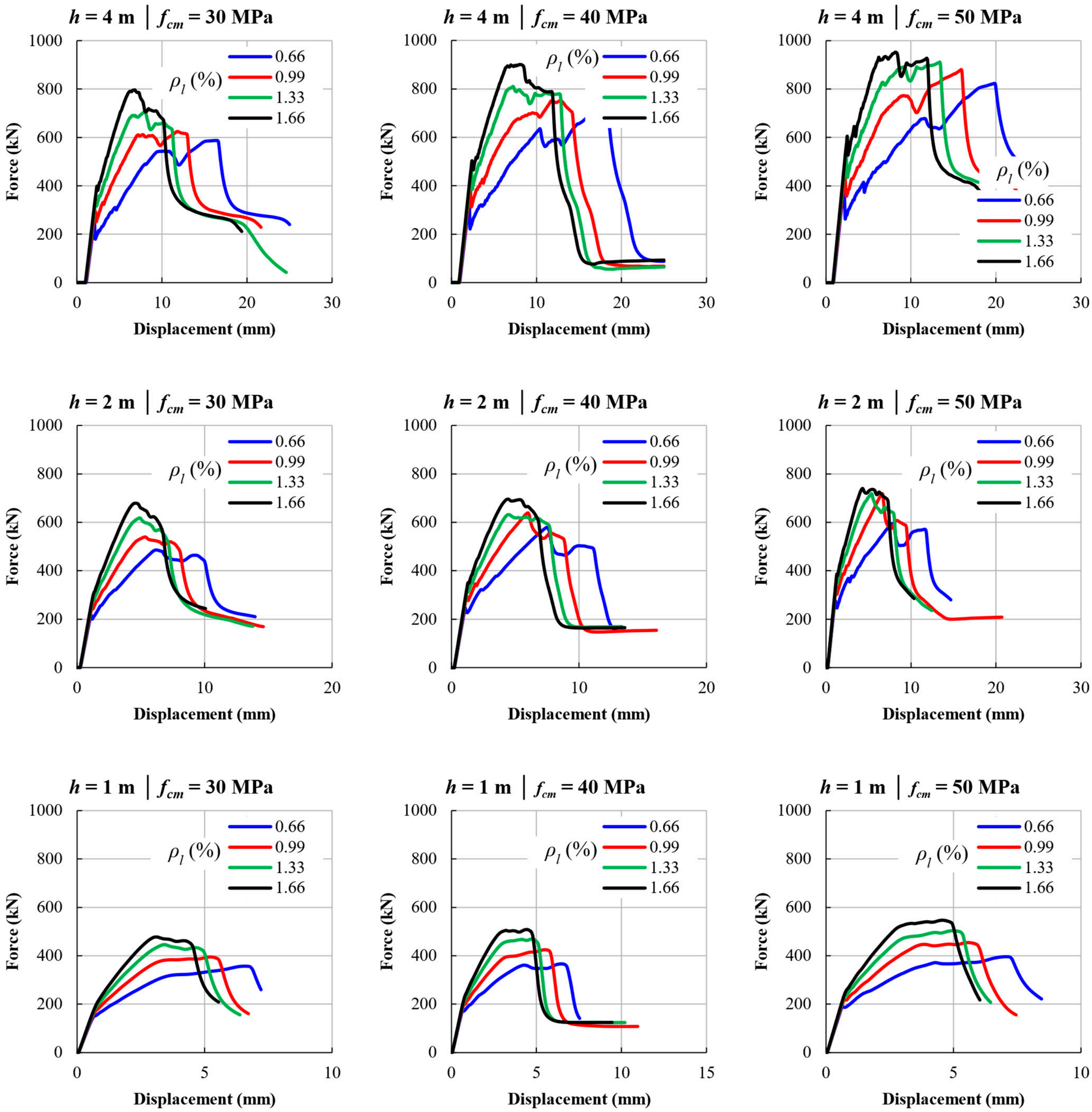

Figure 11. Influence of member depth, concrete compressive strength, and longitudinal reinforcement ratio on the force–displacement response.

Overall, the numerical force–displacement responses reproduce key qualitative features predicted by both CSCT and MCFT, including size-dependent stiffness degradation, strain-controlled shear resistance, and the beneficial yet limited role of increased longitudinal reinforcement in mitigating size effects. The agreement between the observed numerical trends and these well-established shear theories supports the physical consistency of the numerical model and reinforces its suitability for investigating shear-critical behavior in reinforced concrete members.

5.3. Nominal Shear Strength and Size Effect

Figure 12 presents the evolution of the numerically obtained nominal shear strengths $v_{FEM} = \mathrm{V_{FEM}}/(\mathrm{b_w}{\cdot}\mathrm{d})$ as a function of the effective depth d, for different combinations of concrete compressive strength f_{cm} and longitudinal reinforcement ratio ρ_l. The red curves correspond to the calibrated energetic size effect law (SEL Type II) proposed by Bažant [15], fitted to the numerical results following the nonlinear regression procedure proposed by Levenberg–Marquardt. The SEL Type II expression is described by [15]:

$$v(d) = v_0\left(1 + \frac{d}{d_0}\right)^{-1/2} \tag{13}$$

where v_0 represents the asymptotic nominal shear strength for small-scale members (i.e., nominal shear strength that the member would have in the absence of significant size effect), and d_0 is the transitional size parameter governing the shift from plastic behavior to fracture-controlled response (see Figure 1a).

For all investigated configurations, a systematic reduction in nominal shear strength with increasing depth is observed, confirming the presence of a pronounced deterministic size effect. Although the ultimate shear force increases with member size, the nominal shear strength decreases significantly as beam depth grows from approximately 1000 mm to 4000 mm. This behavior is consistent with fracture-mechanics-based interpretations of shear failure in quasi-brittle materials, as originally formalized through the energetic size effect law proposed by Bažant [15].

The reduction in shear strength with increasing depth has been repeatedly confirmed in classical experimental programs on beams without stirrups, including the seminal tests reported by Bažant and Kazemi [12], which provided one of the first systematic validations of the size effect in diagonal shear failure. More recently, Bentz and Buckley [73] repeated and extended these experiments, reinforcing that large members exhibit significantly lower nominal shear resistance than small-scale laboratory specimens.

Comparing subfigures (a–c), (d–f), and (g–i), an increase in concrete compressive strength from 30 MPa to 50 MPa results in only moderate increases in v_0, indicating that concrete strength has a secondary influence compared to member depth. This confirms that shear resistance in large members without stirrups is not solely governed by compression chord capacity, but also by size effect.

Interestingly, the transitional size parameter d_0 tends to increase with higher concrete strength in several cases, suggesting that stronger concretes may delay the onset of fracture-dominated scaling, although the size effect remains significant even at $f_{cm} = 50$ MPa.

The pronounced effect of the longitudinal reinforcement ratio is also evident in Figure 12. As ρ_l increases from 0.66% to 1.33%, the calibrated asymptotic nominal shear strength v_0 increases substantially, reflecting the contribution of flexural reinforcement to shear transfer mechanisms also predicted by the MCFT and CSCT.

Moreover, higher ρ_l values generally lead to improved correlation coefficients (R^2), indicating that the size effect law provides an excellent representation of the numerical results across reinforcement levels. This is consistent with observations that reinforcement ratio affects the reference strain field and critical crack opening, which are central parameters in shear theories such as CSCT [69].

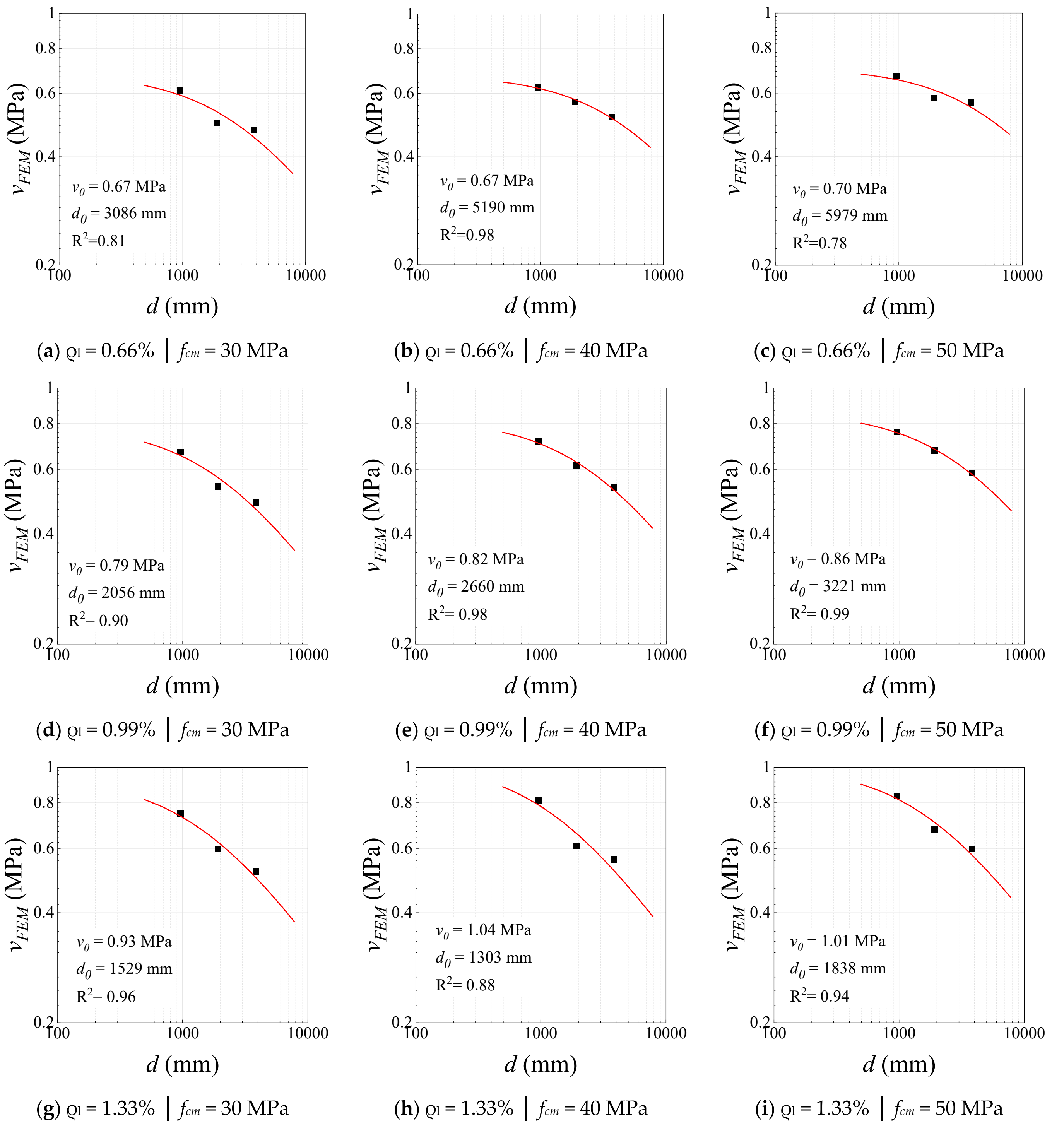

Figure 12. Variation of the numerically obtained nominal shear strength $v_{FEM} = V_{FEM}/(b_w{\cdot}d)$ with effective depth d for beams without transverse reinforcement, considering different longitudinal reinforcement ratios ρ_l and concrete compressive strengths f_{cm}. Red curves represent the calibrated Bažant Size Effect Law (SEL Type II), with fitted parameters v_0 and d_0.

6. Analytical Models to Predict the Shear Capacity

In this study, the FEM predictions of shear capacity were compared to the expressions from four code provisions: EN 1992-1-1:2023 [27], EN 1992-1-1:2005 [74], ACI 318:2019 [26], ACI 318:2014 [75] and fib Model Code 2020 [76]. In addition, the numerical results were also compared to the analytical model proposed by Bažant and Yu [77]. In predictions with these code expressions, the material safety factors such as γ_c were assumed equal to 1 and the characteristic value of compressive strength of concrete f_{ck} was replaced by the average value f_{cm}. This approach is commonly adopted in code assessment studies because it isolates the predictive capability of the mechanical model embedded in the code expressions, avoiding the influence of safety margins intended for structural design. Consequently, the comparisons presented in this study should be interpreted as an evaluation of the accuracy of the code formulations, rather than their conservatism for design purposes. In addition, the loading configuration and geometry of the analyzed members satisfy the main assumptions underlying the code provisions considered, which means that they exhibit shear slenderness associated with slender beams (for non-slender configurations, strut and tie models should be used).

6.1. European Code: EN 1992-1-1:2023 [27]

According to this code, the design value of the shear capacity should be taken as:

$$V_{Rd,c} = \frac{0.66}{\gamma_v} \cdot \left(100 \cdot \rho_l \cdot f_{ck} \cdot \frac{d_{dg}}{d}\right)^{1/3} \cdot b_w \cdot d \geq V_{Rd,\min} \tag{14}$$

$$V_{Rd,\min} = \frac{11}{\gamma_v} \cdot \sqrt{\frac{f_{ck}}{f_{yd}} \cdot \frac{d_{dg}}{d}} \cdot b_w \cdot d \tag{15}$$

where γ_v is the partial factor for shear design; ρ_l is the reinforcement ratio for longitudinal reinforcement; f_{ck} is the characteristic concrete cylinder compressive strength; f_{yd} is the design value of the yield strength, which has been used to design the flexural reinforcement; d is the effective depth of the flexural reinforcement; and b_w is the beam width.

d_{dg} is a size parameter describing the failure zone roughness, which depends on the concrete type and its aggregate properties, which may be taken as:

$$d_{dg} = \begin{cases} 16\ \text{mm} + D_{lower} \leq 40\ \text{mm},\ \text{for } f_{ck} \leq 60\ \text{MPa} \\ 16\ \text{mm}\ +\ \text{D}_{lower} \cdot (60/f_{ck})^2 \leq 40\ \text{mm},\ \text{for } f_{ck} > 60\ \text{MPa} \end{cases} \tag{16}$$

D_{lower} is the smallest value of the upper sieve size D in an aggregate for the coarsest fraction of aggregates in the concrete permitted by the specification of concrete [78]; ρ_l is the reinforcement ratio for bonded longitudinal reinforcement in the tensile zone due to bending referred to the nominal concrete area (=A_{sl}/b_w·d); A_{sl} is the effective area of tensile reinforcement at the distance d beyond the section considered; b_w is the width of the cross-section of linear members.

6.2. European Code EN 1992-1-1:2005

In the European code (EN 1992-1-1:2005), the shear capacity of a reinforced concrete member without stirrups is calculated as:

$$V_{Rd,c} = \max\begin{cases} \left[C_{Rd,c}k(100\rho_l f_{ck})^{1/3} + k_1\sigma_{cp}\right]b_w d \\ (v_{\min} + k_1\sigma_{cp})b_w d \end{cases} \tag{17}$$

$$v_{\min} = 0.035k^{3/2}{f_{ck}}^{1/2} \tag{18}$$

C_{Rdc} = 0.18/γ_c and k_1 = 0.15 for NEN EN 1992-1-1:2005 [74]. k is the size-effect factor that accounts for the reduction of shear strength with increasing effective depth and is calculated as:

$$k = 1 + \sqrt{\frac{200}{d}} \leq 2, \text{ with } d \text{ in mm} \tag{19}$$

σ_{cp} is the concrete compressive stress at the centroidal axis due to axial loading and/or prestressing (σ_{cp} = N_{Ed}/A_c in MPa, N_{Ed} > 0 in compression).

6.3. American Building Code: ACI 318:2019

In the current American code ACI 318:2019, the shear capacity is expressed as:

$$V_{R,c} = \left[0.66\lambda_s \cdot \lambda \cdot (\rho_l)^{1/3}\sqrt{f_{ck}}\right] b_w \cdot d \tag{20}$$

$$\lambda = \begin{cases} 1, \text{ to normalweight aggregate} \\ 0.75, \text{ to lightweight aggregate} \end{cases} \tag{21}$$

$$\lambda_s = \sqrt{\frac{2}{1 + 0.004d}} \leq 1\text{ , with } d \text{ in mm} \tag{22}$$

where λ_s is the size effect factor and λ considers the aggregate density (normal weight or lightweight aggregate).

6.4. American Building Code: ACI 318:2014

According to ACI 318:2014 [75], the concrete shear resistance is calculated using the simplified expression (for non-prestressed members and without axial compression effects):

$$V_{R,c} = 0.17 \cdot \lambda \cdot \sqrt{f_{ck}} \cdot b_w \cdot d \tag{23}$$

where f_{ck} is the specified compressive strength of concrete in MPa, b_w is the effective web width (or slab strip width) in mm, d is the effective depth in mm, and λ is a modification factor accounting for lightweight concrete ($\lambda = 1.0$ for normal-weight concrete).

6.5. *fib* Model Code 2020

According to the *fib* Model 2020 [76], the design shear resistance of a reinforced concrete members without transverse reinforcement may be expressed as:

$$V_{Rd,c} = k_v \cdot \frac{\sqrt{f_{ck}}}{\gamma_c} \cdot b_w \cdot z_v \tag{24}$$

where f_{ck} is given in MPa. For the effective shear depth z_v required for calculating the shear resistance $V_{Rd,c}$, a value of 0.9 d may be assumed.

6.5.1. Level I of Approximation

For members with an effective shear depth $z_v \geq 800$ mm, the value of $\sqrt{f_{ck}}$ is limited to a maximum of 8 MPa. For members without significant axial force, with reinforcement yield strength $f_{yk} \leq 700$ MPa, and a maximum aggregate size not smaller than 10 mm, the shear coefficient k_v can be determined through the Level I approximation as:

$$k_v = \frac{0.4}{1 + 750 \cdot f_{yd}/E_s} \cdot \frac{1300}{1000 + 1.25 \cdot z_v} \tag{25}$$

with z_v expressed in mm and f_{yd} denoting the design yield strength of the longitudinal flexural reinforcement.

6.5.2. Level II of Approximation

For the Level II approximation, the design shear resistance is evaluated as follows:

$$k_v = \frac{0.4}{1 + 1500 \cdot \varepsilon_x} \cdot \frac{1300}{1000 + k_{dg} \cdot z_v} \tag{26}$$

With z_v expressed in mm. In turn, k_{dg} represents the effect of the critical shear crack roughness and is computed as:

$$k_{dg} = \frac{32}{16 + d_g} \geq 0.75 \tag{27}$$

where d_g is the maximum size of the aggregate in mm. In addition, if a member has $z_v \geq 800$ mm and $f_{ck} \geq 70$ MPa or uses lightweight concrete of any strength, k_{dg} = 2.0.

The longitudinal strain ε_x is calculated at the mid-depth of the effective shear depth being considered as follows (in the absence of external normal forces):

$$\varepsilon_x = \frac{1}{2 \cdot E_s \cdot A_s} \cdot \frac{M_{Ed}}{z_v} \tag{28}$$

where M_{Ed} is the design bending moment at the critical section.

6.6. Bažant and Yu [77] Shear Strength Model

According to this model, the shear strength of members without transverse reinforcement is mainly governed by the compressive failure of the concrete in the strut region rather than by a purely empirical shear transfer mechanism. A key assumption of the model is the energetic size effect, originally formulated by Bažant [15], which relates the reduction in nominal shear strength to the increase in structural size through fracture mechanics considerations. Based on these assumptions, the shear strength can be expressed by the following equations:

$$V_{R,c} = 1.104 \cdot {\rho_l}^{3/8} \cdot \left(1 + \frac{d}{a}\right) \cdot \frac{1}{\sqrt{1 + d/d_0}} \cdot \sqrt{f_{cm}} \cdot b_w \cdot d \tag{29}$$

$$d_0 = 639.8 \cdot \sqrt{d_g} \cdot {f_{cm}}^{-2/3} \tag{30}$$

where b_w is the beam width, d is the effective depth of the cross-section. The parameter f_{cm} represents the concrete compressive strength, while ρ_l is the longitudinal reinforcement ratio. The term a corresponds to the shear span, defined as the distance between centers of concentrated load and support. The parameter d_0 is a transitional size parameter that governs the magnitude of the size effect and depends on both the concrete strength and the maximum aggregate size; d_g denotes the maximum aggregate size of the concrete mix. According to the original formulation, the geometric parameters d, d_0 and d_g are expressed in millimeters. The control section to calculate the shear demand was considered at the mid-shear span.

7. Comparison Between the Tested and Predicted Resistances

Figure 13 presents a systematic evaluation of the predictive accuracy of several design provisions and mechanical models for the shear resistance of reinforced concrete members without transverse reinforcement. The comparison is expressed through the ratio V_{FEM}/V_{calc}, where values above unity indicate conservative predictions, whereas values below unity correspond to unconservative estimations of shear capacity. Although the statistical indicators (average value and coefficient of variation) provide useful information regarding the overall predictive accuracy of each formulation, they do not fully capture whether the size-effect trend is properly represented. For this reason, the results in Figure 13 are also analyzed in terms of the variation of V_{FEM}/V_{calc} with the effective depth d. If a formulation correctly represents the size effect, the ratio V_{FEM}/V_{calc} should remain approximately constant along the depth investigated range. Conversely, systematic trends with increasing depth indicate that the formulation does not adequately capture the reduction in nominal shear strength associated with the size effect.

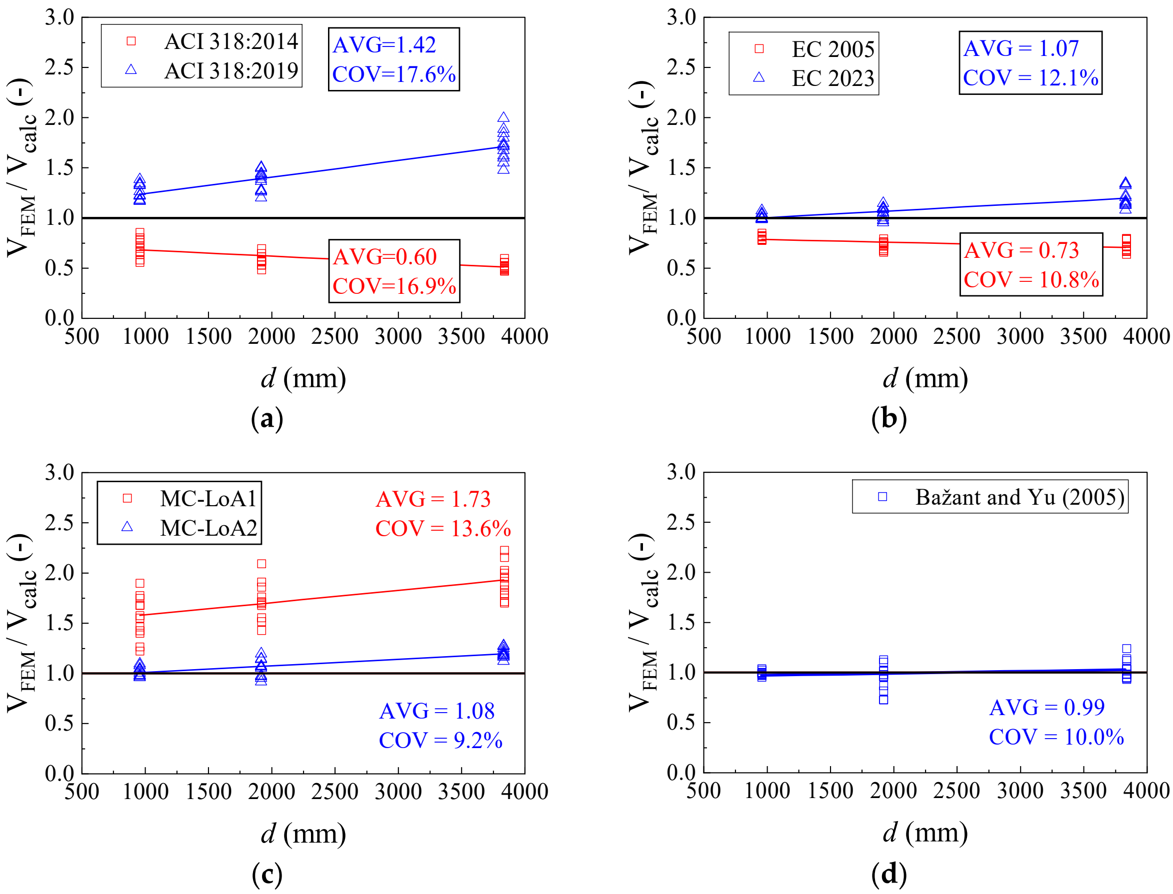

Figure 13. Accuracy of different code provisions for predicting the shear capacity of reinforced concrete beams without transverse reinforcement as a function of effective depth d. The ratios V_{FEM}/V_{calc} are shown for (**a**) ACI 318-2014 and ACI 318-2019; (**b**) EN 1992-1-1:2005 (EC-2005) and EN 1992-1-1:2023 (EC-2023); (**c**) fib Model Code approaches LoA1 and LoA2 (MC-LoA1 and MC-LoA2); and (**d**) Bažant and Yu [77,79].

The comparison between ACI 318-2014 and ACI 318-2019 (Figure 13a) highlights the substantial improvement achieved in the most recent edition of the American code. ACI 318-2014 remains systematically unconservative, with an overall average ratio of 0.60 and moderate scatter (COV = 16.9%), indicating a consistent overestimation of shear strength across all investigated depths. This deficiency becomes increasingly critical for larger members, confirming that the older formulation does not adequately capture the reduction in nominal shear strength associated with the size effect. In contrast, ACI 318-2019 provides consistently conservative predictions, with an overall average ratio of 1.42 and comparable scatter (COV = 17.6%), whose statistics are very similar to the ones shown by Kuchma et al. [29] for another database. This improvement reflects the incorporation of explicit size-effect considerations in the updated code. Nevertheless, the results suggest that ACI 318-2019 may become increasingly conservative for very deep members, potentially penalizing large-scale applications.

A similar trend is observed in the Eurocode provisions (Figure 13b). The EN 1992-1-1:2005 formulation (EC2005) exhibits unconservative predictions, with an overall average ratio of 0.74. Although less severe than ACI 318-2014, this indicates that EC2005 still tends to overestimate the shear resistance of members without stirrups. Moreover, the results reveal a systematic depth-dependent trend: the ratio V_{FEM}/V_{calc} tends to decrease with increasing effective depth d, indicating that the formulation progressively overestimates the shear capacity of larger members. This behavior suggests that the size effect is not adequately captured in the EC2005 expression, particularly in the range of thick members investigated in this study. On the other hand, the updated EN 1992-1-1:2023 (EC2023) shows markedly improved agreement with experimental evidence, yielding an average ratio close to unity (AVG = 1.08) and relatively low scatter (COV = 9.6%). In addition to the improved statistical indicators, the results do not show a pronounced systematic trend with increasing depth, indicating that the formulation is able to reproduce the depth-dependent reduction in nominal shear strength more consistently. This demonstrates that recent Eurocode developments provide a more reliable representation of size-dependent shear behavior, offering both improved safety and greater consistency across different member depths.

The comparison with the *fib* Model Code approaches (Figure 13c) further emphasizes the influence of the adopted safety format. The LoA1 approach is highly conservative, with an overall average ratio of 1.72 and the coefficient of variation equals 13.6%. This indicates, as expected, that MC-LoA1 is more adequate for a preliminary design. In contrast, the LoA2 approach provides very similar predictions to those from EC2023, with an overall average ratio of 1.08 and a coefficient of variation equals 9.2%.

Figure 13d presents the comparison between the numerical results and the predictions obtained using the Bažant and Yu model [77,79]. Overall, the formulation shows very good agreement with the numerical simulations, with an average ratio V_{FEM}/V_{calc} of 0.99 and a coefficient of variation of 10.0%. The results are closely distributed around unity and exhibit a nearly horizontal trend with increasing effective depth d, indicating that the model adequately captures the size effect observed in the numerical simulations over the investigated depth range.

Table 4 describes in more detail the influence of member depth on the predictive performance of shear design models for slender and thick members without stirrups. For the smallest beams ($d = 960$ mm), EC2023 already provides predictions essentially centered around unity (AVG = 1.02), whereas EC2005 remains unconservative (AVG = 0.81). As depth increases to $d = 1920$ mm and $d = 3840$ mm, the limitations of older empirical formulations become more pronounced. Both ACI 318-2014 and EC2005 show decreasing ratios, confirming their inability to capture the strong reduction in nominal shear strength for thick members. Conversely, EC2023 maintains stable predictions with limited scatter, demonstrating superior robustness with respect to member size. The fib Model Code LoA1 becomes progressively more conservative as depth increases (AVG rising from 1.55 to 1.73), while LoA2 remains the closest to experimental results, albeit slightly conservative for the largest members (AVG = 1.19 at $d = 3840$ mm).

In the context of accuracy levels by member thickness, some aspects should be highlighted. For instance, most codes usually do not provide information on the databases used in the calibration or validation of expressions. Because of this, designers may not be aware of the limits of applicability of the available shear expressions. Besides that, in earlier versions of Eurocode and ACI, the shear expressions were semi-empirically calibrated based on available databases. Consequently, the accuracy of such expressions cannot be assured beyond the calibration range. Nevertheless, mechanical-based models such as the ones included in the EN 1992-1-1:2023 [27] and fib Model Code 2020 [76] tend to provide better accuracy even when applied beyond the validated data range.

Table 4. Influence of member depth on the predictive performance of different shear design models for beams without stirrups.

d (mm)		V_{FEM}/V_{calc}	V_{FEM}/V_{calc}	V_{FEM}/V_{calc}	V_{FEM}/V_{calc}	V_{FEM}/V_{calc}	V_{FEM}/V_{calc}	V_{FEM}/V_{calc}
	Code	**ACI 318:2014**	**ACI 318:2019**	**EC 2005**	**EC 2023**	**MC-LoA1**	**MC-LoA2**	**Bažant and Yu**
960	AVG	0.70	1.26	0.81	1.02	1.55	1.01	0.99
	COV	12.8%	6.4%	3.0%	3.0%	13.4%	4.2%	2.3%
1920	AVG	0.58	1.29	0.68	0.98	1.72	1.05	0.94
	COV	9.5%	13.5%	12.4%	12.4%	10.4%	8.1%	13.9%
3840	AVG	0.52	1.71	0.71	1.20	1.92	1.19	1.03
	COV	7.0%	8.6%	7.5%	7.5%	8.7%	3.8%	9.0%
All	AVG	0.60	1.42	0.73	1.07	1.73	1.08	0.99
	COV	16.9%	17.6%	10.8%	12.1%	13.6%	9.2%	10.0%

The results obtained with the Bažant and Yu model [77,79] show a very good agreement with the numerical predictions across the investigated range of member depths. The overall average ratio V_{FEM}/V_{calc} is 0.99 with a coefficient of variation of 10.0%, indicating an almost unbiased prediction and moderate scatter. When the results are examined as a function of member depth, the average ratios remain close to unity, varying from 0.94 to 1.03 for $d = 960$ mm to 3840 mm. This relatively stable behavior suggests that the formulation adequately captures the size effect on shear strength over the investigated depth range.

8. Conclusions

This paper investigated the shear resistance of reinforced concrete beams without transverse reinforcement, focusing on the combined influence of member depth, concrete compressive strength, and longitudinal reinforcement ratio. Nonlinear finite element simulations were performed, and the numerical shear capacities were evaluated against the predictions of major design provisions, including ACI 318:2014, ACI 318:2019, Eurocode 2 (EN 1992-1-1:2005 and EN 1992-1-1:2023), and the fib Model Code approaches LoA1 and LoA2. The conclusions presented below should be considered only within the parameter range investigated. Based on the results obtained, the following conclusions can be drawn:

- The numerical analyses confirmed the presence of a pronounced deterministic size effect in shear (Figure 12). As the effective depth increased, the nominal shear stress at failure decreased systematically, evidencing the transition from a more strength-controlled response in smaller members to a fracture-governed brittle behavior in large-scale beams. This behavior was observed across the entire database, regardless of the reinforcement ratio or concrete compressive strength.
- The depth-dependent trends were consistently represented through the energetic Size Effect Law (SEL Type II) proposed by Bažant [15]. The calibrated parameters v_0 and d_0 provided an excellent fit to the numerical database, demonstrating that non-linear fracture-mechanics-based scaling offers a rational framework for describing shear strength reduction in thick reinforced concrete members failing in shear.
- The concrete compressive strength exerted different influences on the nominal shear strength and asymptotic shear strength, depending on the reinforcement ratio (Figure 12). For slightly reinforced beams (ρ_l = 0.66%), increasing the compressive strength had almost no effect on the asymptotic shear strength (v_0). Nevertheless, increasing concrete compressive strength at higher reinforcement ratios led to a significant increase in the asymptotic shear strength (v_0).

- Significant differences were observed among code predictions. Within the range of parameters investigated in this study and based on the validated numerical models, ACI 318-2014 and EN 1992-1-1:2005 tend to provide unconservative predictions for large member depths, indicating that older empirical formulations do not adequately capture the reduction in nominal shear strength associated with the size effect. The average ratio of numerical to code-calculated resistances was 0.60 for ACI 318:2014 and 0.73 for EN 1992-1-1:2005.
- The updated EN 1992-1-1:2023 formulation showed closer agreement with the numerical results (ratio between numerical and code-based predictions with AVG = 1.07 and COV = 12.1%), yielding predictions near unity with relatively limited scatter. Within the investigated parameter range, these results suggest an improved representation of shear capacity compared with earlier Eurocode formulations.
- The ACI 318:2019 formulation provided consistently conservative predictions of the shear capacity for members without transverse reinforcement within the investigated parameter range. The comparison between the shear resistances obtained from the numerical models and those calculated using the code expressions showed an average ratio of 1.42 with a coefficient of variation of 17.6%. This behavior reflects the incorporation of an explicit size-effect factor in the updated ACI formulation. However, the results also indicate that the level of conservatism tends to increase with member depth, suggesting that the formulation may become increasingly conservative for very large members.
- Among the fib Model Code approaches, which offer alternative calculation options depending on the adopted level of approximation, LoA1 achieved an accuracy comparable to that of the ACI 318:2019 expressions. In contrast, LoA2 provided superior performance compared with the most recent Eurocode version (EN 1992-1-1:2023), yielding nearly unbiased predictions across the full range of effective depths investigated (ratio between numerical and calculated code resistances with AVG = 1.08 and COV = 9.2%).
- Overall, the Bažant and Yu formulation provided accurate predictions of the shear resistance obtained from the numerical simulations. The comparison between numerical and analytical predictions resulted in an overall average ratio V_{FEM}/V_{calc} of 0.99 with a coefficient of variation of 10.0%, indicating an almost unbiased prediction with moderate scatter. This level of agreement reflects the fracture-mechanics basis of the model, which explicitly incorporates the energetic size effect governing shear failure in members without transverse reinforcement.

Overall, the results highlight the importance of accounting for size-effect mechanisms in the assessment of shear capacity of reinforced concrete members without transverse reinforcement, particularly for large structural elements. Nevertheless, further experimental investigations on large-scale specimens would be valuable to complement the numerical findings and further confirm the observed trends.

Author Contributions: Conceptualization, A.M.D.d.S., L.P.P. and E.O.L.L.; methodology, A.M.D.d.S.; software, G.F.G., A.L.S.A. and A.M.D.d.S.; validation, G.F.G. and A.L.S.A.; investigation and resources, G.F.G., A.L.S.A. and A.M.D.d.S.; writing—review and editing, G.F.G. and A.M.D.d.S.; visualization, G.F.G. and A.M.D.d.S.; supervision, A.M.D.d.S., L.P.P., E.O.L.L. and E.F.; project administration, A.M.D.d.S., E.O.L.L. and E.F. All authors have read and agreed to the published version of the manuscript.

Funding: This research was funded by the São Paulo Research Foundation (FAPESP) (Grant number #2024/13561–5, and #2024/19328-0), and São Paulo State University (UNESP) PROPE Edital 03/2025—Programa de Incentivo e Estímulo à Pesquisa aos Recém-contratados—IEPe-RC. This study was also financed in part by the Coordenação de Aperfeiçoamento de Pessoal de Nível Superior—Brasil (CAPES)—Finance Code 001.

Data Availability Statement: The data presented in this study are available on request from the corresponding author.

Acknowledgments: This research was funded in whole or in part by the Fundação para a Ciência e a Tecnologia, I.P. (FCT, https://ror.org/00snfqn58, accessed on 16 February 2026) under Grant UID/6438/2025 (https://doi.org/10.54499/UID/06438/2025, accessed on 16 February 2026) of the research unit CERIS. For the purpose of Open Access, the author has applied a CC-BY public copyright license to any Author's Accepted Manuscript (AAM) version arising from this submission.

Conflicts of Interest: The authors declare no conflicts of interest.

References

1. Bagheri, M.; Ranjbar Malidarreh, N.; Ghaseminejad, V.; Asgari, A. Seismic Resilience Assessment of RC Superstructures on Long–Short Combined Piled Raft Foundations: 3D SSI Modeling with Pounding Effects. *Structures* **2025**, *81*, 110176. [CrossRef]
2. Cao, K.; Fu, Q.; Zhang, J.; Huang, J.; Sun, B.; Ma, W. Damage Evaluation of Gravity Dams Reinforced by Corrugated Steel–Concrete Slab Composite Structures under Underwater near-Field Explosion. *Eng. Fract. Mech.* **2025**, *316*, 110893. [CrossRef]
3. Collins, M.P.; Bentz, E.C.; Quach, P.; Proestos, G.T. The Challenge of Predicting the Shear Strength of Very Thick Slabs. *Concr. Int.* **2015**, *37*, 29–37.
4. de Sousa, A.M.D.; Lantsoght, E.O.L.; El Debs, M.K. Transition between Shear and Punching in Reinforced Concrete Slabs: Review and Predictions with ACI Code Expressions. *ACI Struct. J.* **2023**, *120*, 115. [CrossRef]
5. de Sousa, A.M.D.; Lantsoght, E.O.L.; El Debs, M.K. Shear and Punching Capacity Predictions for One-Way Slabs under Concentrated Loads Considering the Transition between Failure Mechanisms. *Buildings* **2023**, *13*, 434. [CrossRef]
6. de Sousa, A.M.D.; Lantsoght, E.O.L.; Setiawan, A.; El Debs, M.K. Failure Mechanism and Resistance Predictions for One-way Slabs in Transition between Shear and Punching Coupling Linear Elastic Finite Element Analyses with Critical Shear Crack Theory-based Models. *Struct. Concr.* **2026**. [CrossRef]
7. Bui, T.T.; Abouri, S.; Limam, A.; NaNa, W.S.A.; Tedoldi, B.; Roure, T. Experimental Investigation of Shear Strength of Full-Scale Concrete Slabs Subjected to Concentrated Loads in Nuclear Buildings. *Eng. Struct.* **2017**, *131*, 405–420. [CrossRef]
8. Limam, S.; Nana, W.S.A.; Bui, T.T.; Limam, A.; Abouri, S. Experimental Investigation and Analytical Calculations on Shear Strength of Full-Scale RC Slabs with Shear Reinforcement for Nuclear Power Plants. *Nucl. Eng. Des.* **2017**, *324*, 143–157. [CrossRef]
9. Calvi, P.M.; Bentz, E.C.; Collins, M.P. Model for Assessment of Cracked Reinforced Concrete Membrane Elements Subjected to Shear and Axial Loads. *ACI Struct. J.* **2018**, *115*, 501–509. [CrossRef]
10. Jaroslav, H.; Aleksandar, V.; Viktor, B. Failure Analysis of Collapsed Parking Garage Building Due to Punching. *Eng. Fail. Anal.* **2021**, *129*, 105712. [CrossRef]
11. de Sousa, A.M.D.; Lantsoght, E.O.L.; El Debs, M.K. Failure Mechanism of One-Way Slabs under Concentrated Loads after Local Reinforcement Yielding. *Eng. Struct.* **2023**, *291*, 116396. [CrossRef]
12. Bažant, Z.P.; Kazemi, M.T. Size Effect on Diagonal Shear Failure of Beams Without Stirrups. *ACI Struct. J.* **1991**, *88*, 268–276. [CrossRef]
13. de Sousa, A.M.D.; Lantsoght, E.O.L.; El Debs, M.K. One-Way Shear Strength of Wide Reinforced Concrete Members without Stirrups. *Struct. Concr.* **2021**, *22*, 968–992. [CrossRef]
14. Bažant, Z.P.; Kim, J.-K. Size Effect in Shear Failure of Longitudinally Reinforced Beams. *ACI J. Proc.* **1984**, *81*, 456–468. [CrossRef]
15. Bažant, Z.P. Size Effect in Blunt Fracture: Concrete, Rock, Metal. *J. Eng. Mech.* **1984**, *110*, 518–535. [CrossRef]
16. Dönmez, A.; Bažant, Z.P. Size Effect on Punching Strength of Reinforced Concrete Slabs with and without Shear Reinforcement. *ACI Struct. J.* **2017**, *114*, 875–886. [CrossRef]
17. Dönmez, A.; Bažant, Z.P. Critique of Critical Shear Crack Theory for *Fib* Model Code Articles on Shear Strength and Size Effect of Reinforced Concrete Beams. *Struct. Concr.* **2019**, *20*, 1451–1463. [CrossRef]
18. Yu, Q.; Le, J.L.; Hubler, M.H.; Wendner, R.; Cusatis, G.; Bažant, Z.P. Comparison of Main Models for Size Effect on Shear Strength of Reinforced and Prestressed Concrete Beams. *Struct. Concr.* **2016**, *17*, 778–789. [CrossRef]
19. Trandafir, A.N.; Proestos, G.T.; Mihaylov, B.I. Detailed Crack-based Assessment of a 4-m Deep Beam Test Specimen. *Struct. Concrete* **2022**, *24*, 756–770. [CrossRef]
20. Sanabria Díaz, R.A.; Sarmiento Nova, S.J.; Teixeira da Silva, M.C.A.; Mouta Trautwein, L.; de Almeida, L.C. Reliability Analysis of Shear Strength of Reinforced Concrete Deep Beams Using NLFEA. *Eng. Struct.* **2020**, *203*, 109760. [CrossRef]

21. Syroka-Korol, E.; Tejchman, J. Experimental Investigations of Size Effect in Reinforced Concrete Beams Failing by Shear. *Eng. Struct.* **2014**, *58*, 63–78. [CrossRef]
22. Zhai, J.Y.; Moehle, J.P. Shear Strength of Large Beams and Foundations with High-Strength Reinforcement. *Struct. J.* **2026**, *123*, 171–186. [CrossRef]
23. Tan, K.H.; Cheng, G.H. Size Effect on Shear Strength of Deep Beams: Investigating with Strut-and-Tie Model. *J. Struct. Eng.* **2006**, *132*, 673–685. [CrossRef]
24. Mihaylov, B.I.; Bentz, E.C.; Collins, M.P. Two-Parameter Kinematic Theory for Shear Behavior of Deep Beams. *ACI Struct. J.* **2013**, *110*, 447–455. [CrossRef]
25. Reineck, K.-H.; Bentz, E.C.; Fitik, B.; Kuchma, D.A.; Bayrak, O. ACI-DAfStb Database of Shear Tests on Slender Reinforced Concrete Beams without Stirrups. *ACI Struct. J.* **2013**, *110*, 867–876. [CrossRef]
26. *ACI 318-19*; ACI Committee 318 Building Code Requirements for Structural Concrete. American Concrete Institute: Farmington Hills, MI, USA, 2019.
27. *EN 1992-1-1:2023*; Eurocode 2: Design of Concrete Structures. Part 1-1: General Rules and Rules for Building, Bridges and Other Civil Engineering Structures. CEN: Brussels, Belgium, 2023.
28. Belarbi, A.; Kuchma, D.A.; Sanders, D.H. Proposals for New One-Way Shear for the 318 Building Code. *Concr. Int.* **2017**, *39*, 29–70.
29. Kuchma, D.A.; Wei, S.; Sanders, D.H.; Belarbi, A.; Novak, L.C. Development of One-Way Shear Design Provisions of ACI 318-19 for Reinforced Concrete. *ACI Struct. J.* **2019**, *116*, 285–295. [CrossRef]
30. Sigrist, V.; Bentz, E.; Fernández Ruiz, M.; Foster, S.; Muttoni, A. Background to the *Fib* Model Code 2010 Shear Provisions—Part I: Beams and Slabs. *Struct. Concr.* **2013**, *14*, 195–203. [CrossRef]
31. Muttoni, A.; Fernández Ruiz, M.; Cavagnis, F.; Simões, J.T. *Background Document to Clauses 8.2.1 and 8.2.2—Shear in Members without Shear Reinforcement. Background Document for FprEN 1992-1-1*; CEN/TC250/SC2; The European Union: Brussels, Belgium, 2023.
32. Deng, C.; Li, Y.; Xiong, F.; Liu, H.; Li, X.; Zeng, Y. Detection of Rupture Damage Degree in Laminated Rubber Bearings Using a Piezoelectric-Based Active Sensing Method and Hybrid Machine Learning Algorithms. *Struct. Control Health Monit.* **2025**, *2025*, 6694610. [CrossRef]
33. Zhang, J.; Chen, W.; Zhang, J. UAV-Based Quantitative Crack Measurement for Bridges Integrating Four-Point Laser Metric Calibration and Mamba Segmentation. *Autom. Constr.* **2026**, *182*, 106774. [CrossRef]
34. Sandeep, M.S.; Tiprak, K.; Kaewunruen, S.; Pheinsusom, P.; Pansuk, W. Shear Strength Prediction of Reinforced Concrete Beams Using Machine Learning. *Structures* **2023**, *47*, 1196–1211. [CrossRef]
35. Rahman, J.; Ahmed, K.S.; Khan, N.I.; Islam, K.; Mangalathu, S. Data-Driven Shear Strength Prediction of Steel Fiber Reinforced Concrete Beams Using Machine Learning Approach. *Eng. Struct.* **2021**, *233*, 111743. [CrossRef]
36. Castillo, R.; Okumus, P.; Elhami Khorasani, N.; Chandola, V. Machine Learning for Shear Strength of Reinforced-Concrete Beams. *ACI Struct. J.* **2022**, *119*, 83–94. [CrossRef]
37. Solhmirzaei, R.; Salehi, H.; Kodur, V.; Naser, M.Z. Machine Learning Framework for Predicting Failure Mode and Shear Capacity of Ultra High Performance Concrete Beams. *Eng. Struct.* **2020**, *224*, 111221. [CrossRef]
38. Liu, T.; Wang, Z.; Zeng, J.; Wang, J. Machine-Learning-Based Models to Predict Shear Transfer Strength of Concrete Joints. *Eng. Struct.* **2021**, *249*, 113253. [CrossRef]
39. Chen, N.; Li, B.; Wang, Y.; Ying, X.; Wang, L.; Zhang, C.; Guo, Y.; Li, M.; An, W. Motion and Appearance Decoupling Representation for Event Cameras. *IEEE Trans. Image Process.* **2025**, *34*, 5964–5977. [CrossRef]
40. Díaz, R.S.; Nova, S.S.; Trautwein, L.M.; de Almeida, L.C.; Texeira da Silva, M.C.A. Reliability Analysis of a Post-Tensioned Bridge Using NLFEA and Random Fields. In *Bridge Maintenance, Safety, Management, Life-Cycle Sustainability and Innovations*; CRC Press: Boca Raton, FL, USA, 2021; pp. 3747–3754.
41. de Putter, A.; Hendriks, M.A.N.; Rots, J.G.; Yang, Y.; Engen, M.; van den Bos, A.A. Quantification of the Resistance Modeling Uncertainty of 19 Alternative 2D Nonlinear Finite Element Approaches Benchmarked against 101 Experiments on Reinforced Concrete Beams. *Struct. Concr.* **2022**, *23*, 2895–2909. [CrossRef]
42. Luo, W.; Le, J.-L.; Rasoolinejad, M.; Bažant, Z.P. Coefficient of Variation of Shear Strength of RC Beams and Size Effect. *J. Eng. Mech.* **2021**, *147*, 04020144. [CrossRef]
43. Syroka-Korol, E.; Tejchman, J.; Mróz, Z. FE Calculations of a Deterministic and Statistical Size Effect in Concrete under Bending within Stochastic Elasto-Plasticity and Non-Local Softening. *Eng. Struct.* **2013**, *48*, 205–219. [CrossRef]
44. Yang, Y.; Van der Ham, H.; Naaktgeboren, M. Shear Capacity of RC Slab Structures with Low Reinforcement Ratio—An Experimental Aproach. In Proceedings of the Fib Symposium 2021—Lisbon, Lisbon, Portugal, 14–16 June 2021.
45. de Sousa, A.M.D.; Lantsoght, E.O.L.; Genikomsou, A.S.; Prado, L.P.; El Debs, M.K. NLFEA of One-Way Slabs in Transition between Shear and Punching: Recommendations for Modeling. *Eng. Struct.* **2023**, *293*, 116617. [CrossRef]
46. de Sousa, A.M.D.; Lantsoght, E.O.L.; Genikomsou, A.S.; Krahl, P.A.; El Debs, M.K. Behavior and Punching Capacity of Flat Slabs with the Rational Use of UHPFRC: NLFEA and Analytical Predictions. *Eng. Struct.* **2021**, *244*, 112774. [CrossRef]

47. da Silva, M.A.D.R.; de Sousa, A.M.D.; de Lima Araújo, D.; Díaz, R.A.S.; Krahl, P.A.; El Debs, M.K. FEM-Based Practical Recommendations for Detailing UHPC Wet Joints of Precast Slabs. *Structures* **2025**, *80*, 109798. [CrossRef]
48. Dassault Systems Simulia Corp. *Abaqus Analysis User's Manual 6.14*; Dassault Systems Simulia Corp.: Providence, RI, USA, 2014.
49. Lubliner, J.; Oliver, J.; Oller, S.; Oñate, E. A Plastic-Damage Model for Concrete. *Int. J. Solids Struct.* **1989**, *25*, 299–326. [CrossRef]
50. Lee, J.; Fenves, G.L. Plastic-Damage Model for Cyclic Loading of Concrete Structures. *J. Eng. Mech.* **1998**, *124*, 892–900. [CrossRef]
51. Xenos, D.; Grassl, P. Modelling the Failure of Reinforced Concrete with Nonlocal and Crack Band Approaches Using the Damage-Plasticity Model CDPM2. *Finite Elem. Anal. Des.* **2016**, *117–118*, 11–20. [CrossRef]
52. Genikomsou, A.S.; Polak, M.A. Finite Element Analysis of Punching Shear of Concrete Slabs Using Damaged Plasticity Model in ABAQUS. *Eng. Struct.* **2015**, *98*, 38–48. [CrossRef]
53. Henze, L. Querkrafttragverhalten von Stahlbeton-Fahrbahnplatten. PhD Thesis, Institute for Concrete Structures, Technische Universität Hamburg (TUHH), Hamburg, Germany, 2019.
54. Fédération Internationale du Béton (FIB). *Fib Model Code for Concrete Structures 2010*; John Wiley & Sons: Lausanne, Switzerland, 2012; Volume 1–2.
55. Hordijk, D.A. Tensile and Tensile Fatigue Behaviour of Concrete—Experiments, Modelling and Analyses. *Heron* **1992**, *37*, 3–79.
56. Reginato, L.; de Sousa, A.M.D.; Santos, J.V.C.; El Debs, M.K. NLFEA of Reinforced Concrete Corbels: Proposed Framework, Sensibility Study, and Precision Level. *Buildings* **2023**, *13*, 1874. [CrossRef]
57. Wiliam, K.; Warnke, E. Constitutive Model for the Triaxial Behaviour of Concrete. In *Proceedings of the Seminar on Concrete Structures Subjected to Triaxial Stresses*; ISMES: Bergamo, Italy, 1974; pp. 1–30.
58. Kupfer, H.B.; Gerstle, K.H. Behavior of Concrete under Biaxial Stresses. *J. Eng. Mech. Div.* **1973**, *99*, 853–866. [CrossRef]
59. Kupfer, H.B.; Hilsdorf, H.K.; Rusch, H. Behavior of Concrete Under Biaxial Stresses. *ACI J. Proc.* **1969**, *66*, 656–666. [CrossRef]
60. Nana, W.S.A.; Bui, T.T.; Limam, A.; Abouri, S. Experimental and Numerical Modelling of Shear Behaviour of Full-Scale RC Slabs Under Concentrated Loads. *Structures* **2017**, *10*, 96–116. [CrossRef]
61. Neuberger, Y.M.; Andrade, M.V.; de Sousa, A.M.D.; Bandieira, M.; Júnior, E.P.d.S.; dos Santos, H.F.; Catoia, B.; Bolandim, E.A.; Aquino, V.B.d.M.; Christoforo, A.L.; et al. Numerical Analysis of Reinforced Concrete Corbels Using Concrete Damage Plasticity: Sensitivity to Material Parameters and Comparison with Analytical Models. *Buildings* **2023**, *13*, 2781. [CrossRef]
62. Francklin, H.M.; Motta, L.A.d.C.; Reis, E.D.; de Sousa, A.M.D.; Christoforo, A.L.; de Almeida Filho, F.M. Laminated Composite Based on Ramie Fibers as an Alternative Solution for Strengthening Reinforced Concrete Beams. *Compos. B Eng.* **2026**, *312*, 113251. [CrossRef]
63. Díaz, R.S.; Isufi, B.; Trautwein, L.M.; Ramos, A.P. Nonlinear Analysis of Flat Slab-column Connections to Optimize the Use of HPFRC under Monotonic Vertical Loading. *Struct. Concr.* **2022**, *24*, 5787–5807. [CrossRef]
64. Muttoni, A.; Simões, J.T. Shear and Punching Shear According to the Critical Shear Crack Theory: Background, Recent Developments and Integration in Codes. *Rev. IBRACON De Estrut. E Mater.* **2023**, *16*, e16302. [CrossRef]
65. Wosatko, A.; Genikomsou, A.; Pamin, J.; Polak, M.A.; Winnicki, A. Examination of Two Regularized Damage-Plasticity Models for Concrete with Regard to Crack Closing. *Eng. Fract. Mech.* **2018**, *194*, 190–211. [CrossRef]
66. Bažant, Z.P.; Jirásek, M. Nonlocal Integral Formulations of Plasticity and Damage: Survey of Progress. *J. Eng. Mech.* **2002**, *128*, 1119–1149. [CrossRef]
67. Cavagnis, F.; Fernández Ruiz, M.; Muttoni, A. Shear Failures in Reinforced Concrete Members without Transverse Reinforcement: An Analysis of the Critical Shear Crack Development on the Basis of Test Results. *Eng. Struct.* **2015**, *103*, 157–173. [CrossRef]
68. Cavagnis, F.; Fernández Ruiz, M.; Muttoni, A. An Analysis of the Shear-Transfer Actions in Reinforced Concrete Members without Transverse Reinforcement Based on Refined Experimental Measurements. *Struct. Concr.* **2018**, *19*, 49–64. [CrossRef]
69. Muttoni, A.; Fernandez Ruiz, M. Shear Strength of Members without Transverse Reinforcement as Function of Critical Shear Crack Width. *ACI Struct. J.* **2008**, *105*, 163–172. [CrossRef]
70. Bentz, E.C.; Vecchio, F.J.; Collins, M.P. Simplified Modified Compression Field Theory for Calculating Shear Strength of Reinforced Concrete Elements. *ACI Struct. J.* **2006**, *103*, 614–624. [CrossRef]
71. Vecchio, F.J.; Collins, M.P. The Modified Compression-Field Theory for Reinforced Concrete Elements Subjected to Shear. *ACI J. Proc.* **1986**, *83*, 219–231. [CrossRef]
72. Campana, S.; Fernández Ruiz, M.; Anastasi, A.; Muttoni, A. Analysis of Shear-Transfer Actions on One-Way RC Members Based on Measured Cracking Pattern and Failure Kinematics. *Mag. Concr. Res.* **2013**, *65*, 386–404. [CrossRef]
73. Bentz, E.C.; Buckley, S. Repeating a Classic Set of Experiments on Size Effect in Shear of Members without Stirrups. *ACI Struct. J.* **2005**, *102*, 832–838. [CrossRef] [PubMed]
74. *CEN EN 1992-1-1:2005*; Eurocode 2: Design of Concrete Structures -Part 1-1: General Rules and Rules for Buildings. British Standard Institution: London, UK, 2005.
75. *ACI 318-14*; ACI Committee 318 Building Code Requirements for Structural Concrete and Commentary. American Concrete Institute: Farmington Hills, MI, USA, 2014; Volume 11, 6858p.

76. Fédération Internationale du Béton. *Fib Model Code for Concrete Structures 2020*; Fédération Internationale du Béton (FIB): Lausanne, Switzerland, 2023; Volume 1, ISBN 978-2-88394-175-5.
77. Bažant, Z.P.; Yu, Q. Designing Against Size Effect on Shear Strength of Reinforced Concrete Beams Without Stirrups: I. Formulation. *J. Struct. Eng.* **2005**, *131*, 1877–1885. [CrossRef]
78. *BS EN 206*; Concrete Specification, Performance, Production and Conformity. British Standards Institution (BSI): London, UK, 2021.
79. Bažant, Z.P.; Yu, Q. Designing Against Size Effect on Shear Strength of Reinforced Concrete Beams Without Stirrups: II. Verification and Calibration. *J. Struct. Eng.* **2005**, *131*, 1886–1897. [CrossRef]